In-Plane Wave Homogenization and the Emergent Electromomentum Tensor

Paramveer Sharma and Gal Shmuel

Faculty of Mechanical Engineering, Technion–Israel Institute of Technology, Haifa 32000, Israel

Abstract

The electromomentum coupling is a macroscopic interaction between momentum density and electric field in piezoelectric composites, absent from the response of their constituents. Existing works have focused mainly on its analysis scalar mechanical settings. Here, we develop and apply homogenization scheme for the vectorial settings of in-plane motions of periodic composites, where two wave polarizations coexist. The method defines macroscopic fields by ensemble averaging and uses driving sources to obtain a unique effective model for arbitrary frequency and wavevector excitations.

Numerical examples for composites with circular and circular-sector fibers show that the homogenized model recovers the Bloch dispersion of the underlying microstructure while satisfying physical restrictions, whereas equivalent models that suppress electromomentum coupling may violate these restrictions. The structure of the effective properties distinguishes mesoscale effects, present even for axisymmetric cells at finite wavelengths, from symmetry-breaking contributions that persist in the local response of asymmetric cells. Time-domain scattering simulations further demonstrate that the local effective medium reproduces the macroscopic reflected and transmitted response of the underlying composite for the excitations considered. These results advance the modeling and analysis of electromomentum metamaterials, towards their integration in future wave-control applications.

Keywords: Dynamic homogenization, Willis coupling, Electromomentum coupling, Composites, Piezoelectricity, Bloch Waves

1 Introduction

Metamaterials are architectured composites with effective properties that fundamentally differ from the properties of their constituents [1, 2]. Of particular interest are metamaterials for mechanical wave manipulation, finding applications in noise reduction, cloaking, anomalous energy energy transport, and sensing [3–11].

Homogenization theories provide a route to determine the effective properties of composites in terms of their composition [12], usually using some scale separation assumptions and asymptotic expansions

[13–16]. In a series of works, Willis [17–22] pioneered a different paradigm that is free from these approximations, with which he uncovered several counterintuitive wave phenomena. Most notably, Willis showed that the effective stress may depend on the velocity and that the effective momentum may depend on the strain, a dependency that is nonlocal in space in time. These now termed Willis couplings capture additional degrees of freedom for shaping waves [23–27], and are essential for obtaining a physical homogenized description [28–30].

Pernas-Salomón and Shmuel recognized how to generalize Willis' framework to piezoelectric composites, and by doing so theoretically discovered effective cross-couplings of Willis-type between the momentum and electric field; and between the electric displacement and velocity [31]. Subsequently, Shmuel's group and collaborators derived elementary bounds and constraints on the effective properties of materials with such electromomentum couplings [32]; developed a retrieval-based homogenization method [33]; computed the electromomentum tensor of fiber composites at antiplane motion [34]; developed discrete models [35], and maximized the coupling based on topology optimization [36].

The theoretical discovery of the electromomentum coupling has opened fundamental questions and applicational opportunities, motivating efforts to explore both. These efforts include developments of alternative dedicated homogenization and retrieval methods [37–42], bounds [37, 43], optimization [42, 44], studies of resultant anomalous scattering [37, 45–47] and other discrete models [48, 49].

Notwithstanding this recent surge of interest, studies have been mostly limited to one-dimensional media. The only explicit problems that were addressed so far beyond one-dimension where of scalar fields (antiplane shear and pressure fields) in two-dimensional media [34, 37], and an optimization-oriented study of in-plane waves [42]. In the latter, the authors used a finite-element implementation of the homogenization formula that was derived by Pernas-Salomón and Shmuel [31]. Many aspects of in-plane homogenization features, such as Bloch-dispersion recovery, off-dispersion evaluations, physical admissibility and local approximations, were unexplored and are the objective of this work.

Here, we integrate the key ideas of Willis [20], and in turn Pernas-Salomón and Shmuel [31] (see also the thermal analogue derived by Shmuel and Willis [50, 51]), with a plane-wave expansion approach [52–55] to derive the in-plane effective properties of periodic piezoelectric fiber composites. Specifically, we define the effective fields using ensemble averaging [20, 56], which for periodic media reduces to averaging the periodic parts of Bloch–Floquet waves over the unit cell [20, 31, 57]. In addition, Our source-driven approach [29, 39, 58, 59] includes impressed eigenstrain, body force and charge densities so that the effective variables are independent and the effective constitutive operator is uniquely defined [20, 31, 32, 60]. We then employ the Bloch-Floquet theorem and expand the periodic part of the microscopic fields in Fourier series to form an algebraic set of equations. Finally, we manipulate the resultant set to extract the effective operator from the relation between the zero Fourier coefficients of the kinetic and kinematic fields. Conceptually, we mirror the formulation of Muhafra et al. [34]; the essential difference is that the displacement is no longer a scalar field, but instead consists of two coupled components that give rise to two wave polarizations.

We apply our homogenization method for composites that are made of PMMA and PZT–4 phases.

We consider two representative unit cells: one with a circular inclusion and one with a circular-sector inclusion, allowing us to distinguish between features originating from broken symmetries than those from nonlocal effects. The numerical study contains several elements. First, we demonstrate that the homogenized model recovers the Bloch dispersion of the underlying composites. Second, we show that the effective tensors satisfy the reciprocity, energy conservation, and causality restrictions expected of a conservative reciprocal composite, and illustrate how source-free equivalent descriptions that suppress electromomentum coupling may violate these restrictions. Third, we exemplify the ability of the scheme to produce local effective models and to homogenize the response at prescribed frequency–wavevector pairs away from the dispersion surfaces. By comparing circular and circular-sector fibers, we distinguish mesoscale effects, which appear beyond the long-wavelength limit even for axisymmetric cells, from symmetry-breaking contributions that persist in the local response of asymmetric cells. Finally, we test the local effective medium in long-wavelength scattering simulations, showing that it captures the macroscopic reflected and transmitted response of the underlying composite for the excitations considered.

The paper is organized as follows. Section 2 formulates the in-plane piezoelectric fiber composite problem, including the governing equations, source terms, and constitutive structure. Section 3 introduces the ensemble-averaged effective fields and develops the source-driven plane-wave homogenization scheme, leading to the effective relations with Willis and electromomentum cross-couplings. Section 4 presents the numerical analysis: recovery of the Bloch dispersion, verification of reciprocity and energy conservation identities, comparison with equivalent models that suppress electromomentum coupling, evaluation of local and off-dispersion effective properties, and a long-wavelength half-space scattering validation. Section 5 summarizes the main conclusions and outlines directions for extension to three-dimensional and structural electromomentum models.

2 Problem statement

We consider an infinite periodic composite made of piezoelectric fibers embedded in a different piezoelectric matrix. A Cartesian coordinate system is chosen such that the fibers are aligned with the x_3-axis, while the fields vary in the (x_1, x_2)-plane. The composite is driven by time-harmonic sources of the form

$$s(x_1, x_2, t) = s_0\, e^{i(\boldsymbol{\kappa}\cdot\mathbf{x}-\omega t)}, \qquad s = \eta_{11}, \eta_{22}, \eta_{12},\ f_1, f_2,\ q, \tag{1}$$

where $\mathbf{x}$ has the components x_1 and x_2, s_0 is a constant amplitude, ω is the angular frequency, and $\boldsymbol{\kappa}$ is the in-plane wavevector, and $\boldsymbol{\eta}$, $\mathbf{f}$, and q denote impressed eigenstrain, body-force density, and free-charge density, respectively. These sources generate in-plane motion $\mathbf{u}$ with components u_1 and u_2, governed by

$$\nabla\cdot\boldsymbol{\sigma} + \mathbf{f} = \dot{\mathbf{p}}, \qquad \nabla\cdot\mathbf{D} = q, \qquad \nabla\times\mathbf{E} = \mathbf{0}, \tag{2}$$

where $\boldsymbol{\sigma}$ is the Cauchy stress, $\mathbf{p}$ is the momentum density, $\mathbf{D}$ is the electric displacement, and $\mathbf{E}$ is the electric field. The last equation is satisfied identically by introducing an electric potential ϕ, such that $\mathbf{E} = -\nabla\phi$. The local constitutive relations then read

$$\begin{pmatrix} \sigma \\ \mathbf{D} \\ \mathbf{p} \end{pmatrix} = \begin{pmatrix} \mathbf{C} & \mathbf{B}^{\mathsf{T}} & \mathbf{0} \\ \mathbf{B} & -\mathbf{A} & \mathbf{0} \\ \mathbf{0} & \mathbf{0} & \rho \end{pmatrix} \begin{pmatrix} \nabla_{\mathrm{s}}\mathbf{u} - \eta \\ \nabla\phi \\ \dot{\mathbf{u}} \end{pmatrix}, \tag{3}$$

where ρ, $\mathbf{A}$, $\mathbf{B}$, and $\mathbf{C}$ are the mass density, dielectric tensor, piezoelectric tensor, and elasticity tensor, respectively. These properties are piecewise constant in the matrix and fiber phases and periodic over the unit cell. The objective is to determine the constitutive relations between the corresponding macroscopic or effective fields, in some appropriate sense.

3 Dynamic in-plane homogenization method

We follow Refs. [20, 31, 59] and define the macroscopic fields by ensemble averaging. For periodic media, this definition reduces to averaging the periodic part of the Bloch–Floquet field over the unit cell. Specifically, if

$$\zeta(\mathbf{x}, t) = \hat{\zeta}(\mathbf{x})\, e^{\,i(\boldsymbol{\kappa}\cdot\mathbf{x} - \omega t)}, \qquad \hat{\zeta} \text{ is } \Omega\text{-periodic}, \tag{4}$$

then

$$\langle\zeta\rangle(\mathbf{x}, t) = \bar{\zeta}\, e^{\,i(\boldsymbol{\kappa}\cdot\mathbf{x} - \omega t)}, \qquad \bar{\zeta} = |\Omega|^{-1} \int_{\Omega} \hat{\zeta}(\mathbf{x})\, \mathrm{d}\mathbf{x}. \tag{5}$$

This definition filters out the fast periodic oscillations and yields effective fields that satisfy the macroscopic balance equations exactly [21, 60]. The homogenization objective is therefore to determine the relation between the averaged kinetic vector $\langle \mathsf{h} \rangle$ and the averaged kinematic vector $\langle \mathsf{g} \rangle$, where

$$\mathsf{g} := \mathsf{J}\mathsf{w} - \mathsf{m}. \tag{6}$$

To this end, we first write Eq. (3) in the form

$$\mathsf{h} = \mathsf{L}(\mathbf{x})\big(\mathsf{J}\mathsf{w} - \mathsf{m}\big), \tag{7}$$

where

$$\mathsf{h} := \begin{pmatrix} \sigma_{11} \\ \sigma_{22} \\ \sigma_{12} \\ D_1 \\ D_2 \\ p_1 \\ p_2 \end{pmatrix}, \qquad \mathsf{w} := \begin{pmatrix} u_1 \\ u_2 \\ \phi \end{pmatrix}, \qquad \mathsf{m} := \begin{pmatrix} \eta_{11} \\ \eta_{22} \\ \eta_{12} \\ 0 \\ 0 \\ 0 \\ 0 \end{pmatrix}, \tag{8}$$

and

$$\mathsf{J}\mathsf{w} := \begin{pmatrix} u_{1,1} \\ u_{2,2} \\ u_{1,2} + u_{2,1} \\ \phi_{,1} \\ \phi_{,2} \\ -i\omega u_1 \\ -i\omega u_2 \end{pmatrix}, \qquad \mathsf{L}(\mathbf{x}) := \begin{pmatrix} \mathsf{C}(\mathbf{x}) & \mathsf{B}^{\mathsf{T}}(\mathbf{x}) & \mathsf{0}_{3\times2} \\ \mathsf{B}(\mathbf{x}) & -\mathsf{A}(\mathbf{x}) & \mathsf{0}_{2\times2} \\ \mathsf{0}_{2\times3} & \mathsf{0}_{2\times2} & \rho(\mathbf{x})\mathsf{I}_2 \end{pmatrix}. \tag{9}$$

Here the assumed time-harmonic dependence has been used to replace time differentiation by multiplication by $-i\omega$. We substitute the Bloch–Floquet form into Eq. (7) and expand the periodic functions in Fourier series,

$$\hat{\zeta}(\mathbf{x}) = \sum_{\mathbf{G}} \breve{\zeta}_{\mathbf{G}}\, e^{i\mathbf{G}\cdot\mathbf{x}}, \qquad \breve{\zeta}_{\mathbf{G}} := |\Omega|^{-1} \int_{\Omega} \hat{\zeta}(\mathbf{x})\, e^{-i\mathbf{G}\cdot\mathbf{x}}\, \mathrm{d}\mathbf{x}, \tag{10}$$

where $\{\mathbf{G}\}$ is the infinite set of reciprocal in-plane lattice vectors. Projection of the resulting Fourier series onto the harmonic $e^{i\mathbf{G}\cdot\mathbf{x}}$ gives

$$\begin{pmatrix} \breve{\sigma}_{11,\mathbf{G}} \\ \breve{\sigma}_{22,\mathbf{G}} \\ \breve{\sigma}_{12,\mathbf{G}} \\ \breve{D}_{1,\mathbf{G}} \\ \breve{D}_{2,\mathbf{G}} \\ \breve{p}_{1,\mathbf{G}} \\ \breve{p}_{2,\mathbf{G}} \end{pmatrix} = \sum_{\mathbf{G}'} \breve{\mathsf{L}}_{\mathbf{G}\mathbf{G}'} \begin{pmatrix} i(\kappa_1 + G_1')\,\breve{u}_{1,\mathbf{G}'} - \breve{\eta}_{11,\mathbf{G}'} \\ i(\kappa_2 + G_2')\,\breve{u}_{2,\mathbf{G}'} - \breve{\eta}_{22,\mathbf{G}'} \\ i(\kappa_2 + G_2')\,\breve{u}_{1,\mathbf{G}'} + i(\kappa_1 + G_1')\,\breve{u}_{2,\mathbf{G}'} - \breve{\eta}_{12,\mathbf{G}'} \\ i(\kappa_1 + G_1')\,\breve{\phi}_{\mathbf{G}'} \\ i(\kappa_2 + G_2')\,\breve{\phi}_{\mathbf{G}'} \\ -i\omega\,\breve{u}_{1,\mathbf{G}'} \\ -i\omega\,\breve{u}_{2,\mathbf{G}'} \end{pmatrix}, \tag{11}$$

where $\breve{\mathsf{L}}_{\mathbf{G}\mathbf{G}'}$ denotes the Fourier coefficient of $\mathsf{L}(\mathbf{x})$ associated with the basis function $e^{i(\mathbf{G}-\mathbf{G}')\cdot\mathbf{x}}$, or equivalently $\breve{\mathsf{L}}_{\mathbf{G}\mathbf{G}'} = \breve{\mathsf{L}}_{\mathbf{G}-\mathbf{G}'}$. This convolution form follows from the orthogonality of the Fourier functions: after multiplication by $e^{-i\mathbf{G}\cdot\mathbf{x}}$ and integration over the unit cell, only combinations of material and field harmonics whose sum equals the projected reciprocal vector remain.

Eq. (11) can be written compactly as

$$\breve{\mathsf{h}}_{\mathbf{G}} = \sum_{\mathbf{G}'} \breve{\mathsf{L}}_{\mathbf{G}\mathbf{G}'}\Big(\mathsf{J}_{\mathbf{G}'}\,\breve{\mathsf{w}}_{\mathbf{G}'} - \breve{\mathsf{m}}_{\mathbf{G}'}\Big), \tag{12}$$

where

$$\breve{\mathsf{h}}_{\mathbf{G}} = \begin{pmatrix} \breve{\sigma}_{11,\mathbf{G}} \\ \breve{\sigma}_{22,\mathbf{G}} \\ \breve{\sigma}_{12,\mathbf{G}} \\ \breve{D}_{1,\mathbf{G}} \\ \breve{D}_{2,\mathbf{G}} \\ \breve{p}_{1,\mathbf{G}} \\ \breve{p}_{2,\mathbf{G}} \end{pmatrix}, \qquad \breve{\mathsf{w}}_{\mathbf{G}} = \begin{pmatrix} \breve{u}_{1,\mathbf{G}} \\ \breve{u}_{2,\mathbf{G}} \\ \breve{\phi}_{\mathbf{G}} \end{pmatrix}, \qquad \breve{\mathsf{m}}_{\mathbf{G}} = \begin{pmatrix} \breve{\eta}_{11,\mathbf{G}} \\ \breve{\eta}_{22,\mathbf{G}} \\ \breve{\eta}_{12,\mathbf{G}} \\ 0 \\ 0 \\ 0 \\ 0 \end{pmatrix}, \tag{13}$$

and

$$\mathsf{J}_{\mathbf{G}} := \begin{pmatrix} i(\kappa_1 + G_1) & 0 & 0 \\ 0 & i(\kappa_2 + G_2) & 0 \\ i(\kappa_2 + G_2) & i(\kappa_1 + G_1) & 0 \\ 0 & 0 & i(\kappa_1 + G_1) \\ 0 & 0 & i(\kappa_2 + G_2) \\ -i\omega & 0 & 0 \\ 0 & -i\omega & 0 \end{pmatrix}. \tag{14}$$

Having obtained a useful Fourier representation of the constitutive equations, we proceed to rewrite the governing in-plane equations in the same form. These equations are

$$\sigma_{11,1}(\mathbf{x},t) + \sigma_{12,2}(\mathbf{x},t) + f_1(\mathbf{x},t) = -i\omega\, p_1(\mathbf{x},t), \tag{15a}$$

$$\sigma_{12,1}(\mathbf{x},t) + \sigma_{22,2}(\mathbf{x},t) + f_2(\mathbf{x},t) = -i\omega\, p_2(\mathbf{x},t), \tag{15b}$$

$$D_{1,1}(\mathbf{x},t) + D_{2,2}(\mathbf{x},t) = q(\mathbf{x},t). \tag{15c}$$

Using the Bloch–Floquet form, expanding the periodic parts in Fourier series, and again applying orthogonality gives, for each $\mathbf{G}$,

$$i(\kappa_1 + G_1)\breve{\sigma}_{11,\mathbf{G}} + i(\kappa_2 + G_2)\breve{\sigma}_{12,\mathbf{G}} + \breve{f}_{1,\mathbf{G}} = -i\omega\, \breve{p}_{1,\mathbf{G}}, \tag{16a}$$

$$i(\kappa_1 + G_1)\breve{\sigma}_{12,\mathbf{G}} + i(\kappa_2 + G_2)\breve{\sigma}_{22,\mathbf{G}} + \breve{f}_{2,\mathbf{G}} = -i\omega\, \breve{p}_{2,\mathbf{G}}, \tag{16b}$$

$$i(\kappa_1 + G_1)\breve{D}_{1,\mathbf{G}} + i(\kappa_2 + G_2)\breve{D}_{2,\mathbf{G}} = \breve{q}_{\mathbf{G}}. \tag{16c}$$

We write Eq. (16) compactly as

$$\mathsf{D}_{\mathbf{G}}^{\mathsf{T}}\,\breve{\mathsf{h}}_{\mathbf{G}} = -\breve{\mathsf{f}}_{\mathbf{G}}, \tag{17}$$

where

$$\mathsf{D}_{\mathbf{G}} = \begin{pmatrix} i(\kappa_1+G_1) & 0 & 0 \\ 0 & i(\kappa_2+G_2) & 0 \\ i(\kappa_2+G_2) & i(\kappa_1+G_1) & 0 \\ 0 & 0 & i(\kappa_1+G_1) \\ 0 & 0 & i(\kappa_2+G_2) \\ i\omega & 0 & 0 \\ 0 & i\omega & 0 \end{pmatrix}, \qquad \breve{\mathsf{f}}_{\mathbf{G}} = \begin{pmatrix} \breve{f}_{1,\mathbf{G}} \\ \breve{f}_{2,\mathbf{G}} \\ -\breve{q}_{\mathbf{G}} \end{pmatrix}. \tag{18}$$

Next, we collect the equations corresponding to all reciprocal lattice vectors $\mathbf{G}$ and write them as the single infinite matrix system

$$\mathsf{D}_A^{\mathsf{T}}\,\mathsf{h}_A = -\mathsf{f}_A, \qquad \mathsf{h}_A = \mathsf{L}_A\big(\mathsf{J}_A\mathsf{w}_A - \mathsf{m}_A\big). \tag{19}$$

In the numerical examples below, this infinite-dimensional algebraic system is truncated to a finite number of plane waves. If the number of retained reciprocal vectors is N, then f_A has $3N$ components, h_A has $7N$ components, D_A and J_A are $7N \times 3N$ matrices, L_A is a $7N \times 7N$ matrix, w_A has $3N$ components, and m_A has $7N$ components.

The final stage is to extract the average fields and thereby identify the effective operator. It follows from Eq. (19) that the zeroth Fourier coefficient of h, which is the amplitude of the effective kinetic field $\langle \mathsf{h} \rangle$, can be written as

$$\bar{\mathsf{h}} := \begin{pmatrix} \bar{\sigma}_{11} \\ \bar{\sigma}_{22} \\ \bar{\sigma}_{12} \\ \bar{D}_1 \\ \bar{D}_2 \\ \bar{p}_1 \\ \bar{p}_2 \end{pmatrix} \equiv \begin{pmatrix} \breve{\sigma}_{11,0} \\ \breve{\sigma}_{22,0} \\ \breve{\sigma}_{12,0} \\ \breve{D}_{1,0} \\ \breve{D}_{2,0} \\ \breve{p}_{1,0} \\ \breve{p}_{2,0} \end{pmatrix} = \mathsf{L}_0\big\{\mathsf{J}_0\bar{\mathsf{w}} - \bar{\mathsf{m}}\big\} + \mathsf{L}_s\mathsf{J}_s\mathsf{w}_s, \tag{20}$$

where subscript 0 denotes blocks associated with $\mathbf{G} = \mathbf{0}$, and subscript s denotes the remaining blocks associated with $\mathbf{G} \neq \mathbf{0}$. Similarly,

$$\bar{\mathsf{w}} := \begin{pmatrix} \bar{u}_1 \\ \bar{u}_2 \\ \bar{\phi} \end{pmatrix} \equiv \begin{pmatrix} \breve{u}_{1,0} \\ \breve{u}_{2,0} \\ \breve{\phi}_0 \end{pmatrix}, \qquad \bar{\mathsf{m}} := \begin{pmatrix} \bar{\eta}_{11} \\ \bar{\eta}_{22} \\ \bar{\eta}_{12} \\ 0 \\ 0 \\ 0 \\ 0 \end{pmatrix} \equiv \begin{pmatrix} \breve{\eta}_{11,0} \\ \breve{\eta}_{22,0} \\ \breve{\eta}_{12,0} \\ 0 \\ 0 \\ 0 \\ 0 \end{pmatrix}. \tag{21}$$

To eliminate the fluctuating part w_s, we first reorder the assembled unknowns such that the $\mathbf{G} = \mathbf{0}$ terms appear first. Since the prescribed sources in Eq. (1) have constant periodic amplitudes, their Fourier expansions contain only a $\mathbf{G} = \mathbf{0}$ component. Thus,

$$\mathsf{w}_A = \begin{pmatrix} \bar{\mathsf{w}} \\ \mathsf{w}_s \end{pmatrix}, \qquad \mathsf{m}_A = \begin{pmatrix} \bar{\mathsf{m}} \\ 0 \end{pmatrix}, \qquad \mathsf{f}_A = \begin{pmatrix} \bar{\mathsf{f}} \\ 0 \end{pmatrix}. \tag{22}$$

We then define

$$\mathsf{Q} := \mathsf{D}_A^{\mathsf{T}} \mathsf{L}_A \mathsf{J}_A, \qquad \mathsf{b} := \mathsf{D}_A^{\mathsf{T}} \mathsf{L}_A \mathsf{m}_A - \mathsf{f}_A, \tag{23}$$

so that Eq. (19) reads

$$\mathsf{Q}\mathsf{w}_A = \mathsf{b}. \tag{24}$$

Using the same decomposition for the rows and columns of Q, we obtain

$$\begin{pmatrix} \mathsf{Q}_{00} & \mathsf{Q}_{0s} \\ \mathsf{Q}_{s0} & \mathsf{Q}_{ss} \end{pmatrix} \begin{pmatrix} \bar{\mathsf{w}} \\ \mathsf{w}_s \end{pmatrix} = \begin{pmatrix} \mathsf{b}_0 \\ \mathsf{b}_s \end{pmatrix}. \tag{25}$$

The second block row gives

$$\mathsf{Q}_{ss}\mathsf{w}_s = \mathsf{b}_s - \mathsf{Q}_{s0}\bar{\mathsf{w}}. \tag{26}$$

Because the sources have only a $\mathbf{G} = \mathbf{0}$ Fourier coefficient,

$$\mathsf{b}_s = (\mathsf{D}_A^{\mathsf{T}} \mathsf{L}_A)_{s0} \bar{\mathsf{m}}, \qquad \mathsf{Q}_{s0}\bar{\mathsf{w}} = (\mathsf{D}_A^{\mathsf{T}} \mathsf{L}_A)_{s0} \mathsf{J}_0 \bar{\mathsf{w}}. \tag{27}$$

Defining

$$\mathsf{Q}_s := \mathsf{Q}_{ss}, \qquad \mathsf{T} := (\mathsf{D}_A^{\mathsf{T}} \mathsf{L}_A)_{s0}, \tag{28}$$

we obtain

$$\mathsf{Q}_s \mathsf{w}_s = -\mathsf{T}\{\mathsf{J}_0\bar{\mathsf{w}} - \bar{\mathsf{m}}\}, \qquad \mathsf{w}_s = -\mathsf{Q}_s^{-1}\mathsf{T}\{\mathsf{J}_0\bar{\mathsf{w}} - \bar{\mathsf{m}}\}. \tag{29}$$

Substituting Eq. (29) into Eq. (20) gives the effective constitutive relation

$$\bar{\mathsf{h}} = \left(\mathsf{L}_0 - \mathsf{L}_s \mathsf{J}_s \mathsf{Q}_s^{-1} \mathsf{T}\right)\{\mathsf{J}_0\bar{\mathsf{w}} - \bar{\mathsf{m}}\} =: \tilde{\mathsf{L}}\{\mathsf{J}_0\bar{\mathsf{w}} - \bar{\mathsf{m}}\}. \tag{30}$$

The effective blocks are identified as

$$\tilde{\mathsf{L}} =: \begin{pmatrix} \tilde{\mathsf{C}} & \tilde{\mathsf{B}}^{\dagger} & \tilde{\mathsf{S}} \\ \tilde{\mathsf{B}} & -\tilde{\mathsf{A}} & \tilde{\mathsf{W}} \\ \tilde{\mathsf{S}}^{\dagger} & \tilde{\mathsf{W}}^{\dagger} & \tilde{\boldsymbol{\rho}} \end{pmatrix}, \tag{31}$$

where $\tilde{\mathsf{S}}$ and $\tilde{\mathsf{S}}^{\dagger}$ are the matrix representations of the Willis couplings, and $\tilde{\mathsf{W}}$ and $\tilde{\mathsf{W}}^{\dagger}$ are the matrix representations of the electromomentum couplings. Since $\tilde{\mathsf{L}}$ depends on ω and $\boldsymbol{\kappa}$, it represents a generally nonlocal operator in time and space. The source-driven construction allows this operator to be evaluated off the dispersion surfaces, because ω and $\boldsymbol{\kappa}$ are prescribed independently by the sources.

4 Numerical analysis

We now evaluate the effective operator derived in Sec. 3 for representative piezoelectric fiber composites and analyze the macroscopic description that it defines. First, we show that the homogenized model recovers the Bloch dispersion of the underlying composites. Second, we evaluate the effective properties both on and off the dispersion surfaces, and verify that they satisfy the reciprocity, energy conservation, and causality restrictions expected of a conservative reciprocal composite. Third, we derive source-free equivalent descriptions that suppress explicit electromomentum coupling, to show they may fail in satisfying these restrictions sufficient criterion for physical admissibility. Finally, we test the local long-wavelength limit of the homogenized medium in a finite-domain time-domain scattering problem.

We consider two square periodic cells of side length $a = 5\,\mathrm{mm}$. The first contains a centered circular inclusion of radius $R = 1.9\,\mathrm{mm}$, i.e., $R/a = 0.38$, and is geometrically inversion symmetric. The second contains a circular-sector inclusion with the same outer radius, zero inner radius, and angular interval $0^\circ \le \theta \le 45^\circ$, where θ is measured from the positive x_1-axis. This geometry breaks inversion symmetry and enables us to distinguish effects associated with dynamic nonlocality from those activated by broken spatial symmetry. The constituent materials are PMMA for the matrix and PZT–4 for the inclusions. The PZT–4 poling direction is aligned with the global x_2-axis; equivalently, the local material 3-direction of PZT–4 is taken parallel to the global x_2-axis. The plane-wave expansion is truncated using $G_{\max} = 7$ so that we retain $N_G = (2G_{\max} + 1)^2 = 225$ reciprocal lattice vectors.

The constituent properties are listed in Table 1 in the local material frame. Here and henceforth, uppercase indices denote Voigt components. Thus, for example, C_{1111} is denoted by C_{11}, a general component is written as C_{IJ}, B_{i12} is denoted by B_{i6} and so on.

4.1 Free waves

We begin with normal modes, namely free Bloch waves in the absence of driving sources (eigenstrain, body force, and free charge). The source-driven formulation provides the effective operator $\tilde{\mathsf{L}}(\omega, \boldsymbol{\kappa})$ for prescribed frequency–wavevector pairs, including pairs that do not satisfy a free-wave condition. To recover the dispersion relation, we substitute this operator into the source-free ensemble-averaged governing equations and seek pairs $(\omega, \boldsymbol{\kappa})$ for which nontrivial averaged amplitudes exist. After eliminating the electric potential, this condition takes the form of a 2×2 compatibility equation acting on the average in-plane displacement components $\bar{u}_1$ and $\bar{u}_2$,

$$\det \mathsf{K}_{\mathrm{red}}\big(\omega, \boldsymbol{\kappa}; \tilde{\mathsf{L}}(\omega, \boldsymbol{\kappa})\big) = 0, \tag{32}$$

Table 1: Constituent material data in the local material frame, written in standard Voigt notation. For the PZT–4 inclusion, the local 3-direction is the poling direction. Only nonzero independent components are listed; the remaining components follow from the usual minor/major symmetries and material symmetry.

Property	PMMA matrix	PZT–4 inclusion
Mass density [$\mathrm{kg\,m^{-3}}$]	1180	7650
Elasticity tensor [GPa]	$C_{11} = C_{22} = C_{33} = 6.2143$ $C_{12} = C_{13} = C_{23} = 4.1429$ $C_{44} = C_{55} = C_{66} = 1.0357$	$C_{11} = C_{22} = 139,\ C_{33} = 115$ $C_{12} = 77.8,\ C_{13} = C_{23} = 74.3$ $C_{44} = C_{55} = 25.6,\ C_{66} = 30.6$
Piezoelectric tensor [$\mathrm{C\,m^{-2}}$]	0	$B_{31} = B_{32} = -5.2,\ B_{33} = 15.1$ $B_{15} = 12.7,\ B_{24} = 12.7$
Dielectric tensor [$\mathrm{F\,m^{-1}}$]	$A_{11} = A_{22} = A_{33} = 2.6562 \times 10^{-11}$	$A_{11} = A_{22} = 6.4501 \times 10^{-9}$ $A_{33} = 5.6196 \times 10^{-9}$

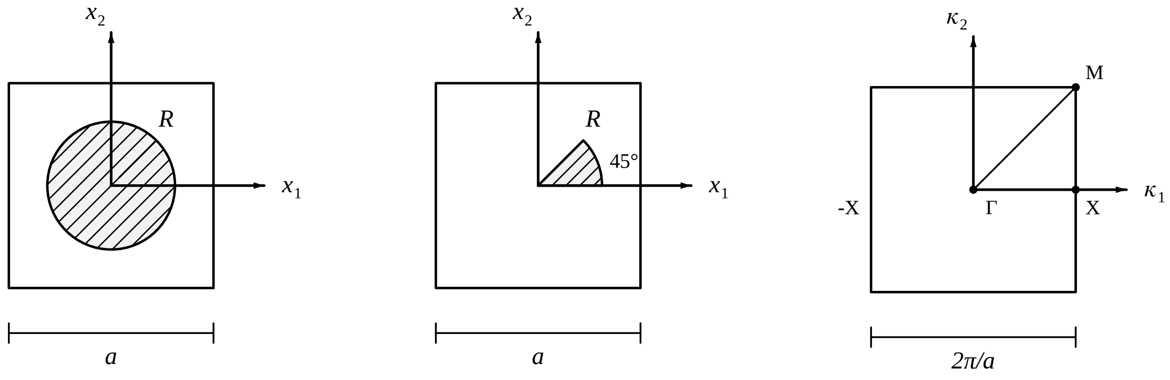

(a) (b) (c)

Figure 1: Geometry and first Brillouin zone for the in-plane piezoelectric composite: (a) square unit cell with circular inclusion, (b) square unit cell with circular-sector inclusion, and (c) first Brillouin zone with the high-symmetry points Γ, X, and M.

where K_{red} is derived in Appendix A. Although the explicit time-harmonic factors enter this condition through powers of ω, the coefficient matrices themselves depend on $(\omega, \boldsymbol{\kappa})$ through the nonlocal effective properties. The dispersion problem is therefore nonlinear in ω, rather than a standard quadratic eigenvalue problem with fixed coefficients, because the effective operator $\tilde{\mathsf{L}}(\omega, \boldsymbol{\kappa})$ depends on the frequency being recovered.[1] This matrix character is one of the distinguishing features of the in-plane formulation: unlike the single-polarization antiplane problem, two coupled elastic wave polarizations remain active, and the free-wave condition must be interpreted as a compatibility condition for the average displacement vector

---

[1] In the numerical recovery, each homogenized branch is recovered locally from the corresponding microstructural seed frequency ω_{seed}. For a prescribed $\boldsymbol{\kappa}$, we evaluate $\tilde{\mathsf{L}}$ at $(\omega_{\text{seed}}, \boldsymbol{\kappa}_{\text{eff}})$, where $\boldsymbol{\kappa}_{\text{eff}} = \pm\boldsymbol{\kappa} + \mathbf{G}$ and $\mathbf{G}$ is a reciprocal-lattice vector. With this evaluated operator held fixed, the reduced compatibility condition is solved as a 2×2 quadratic eigenvalue problem in ω. The accepted recovered root is the positive nearly real root closest to ω_{seed}, subject to residual and branch-continuity checks.

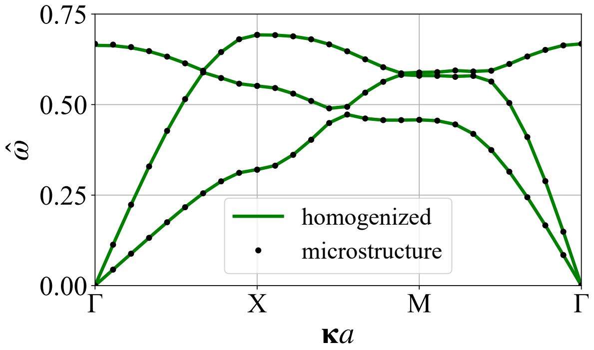

Figure 2: Bloch dispersion of the circular-inclusion composite along Γ–X–M–Γ. Symbols denote the spectrum of the underlying microstructure, and solid curves denote the branches recovered from the homogenized operator.

field.

Fig. 2 presents the first three in-plane Bloch branches of the circular-inclusion composite along the high-symmetry path Γ–X–M–Γ. The circle marks denote the spectrum computed from the underlying microstructure, while the solid curves are obtained from the homogenized model through Eq. (32). The two acoustic branches emanating from Γ correspond to quasi-transverse and quasi-longitudinal polarizations, while the third branch is the first optical Bloch branch. The normalized frequency is

$$\hat{\omega} = \frac{\omega a}{2\pi c_s^{(m)}}, \qquad c_s^{(m)} = \sqrt{\mu^{(m)}/\rho^{(m)}}, \tag{33}$$

where $c_s^{(m)}$ is the shear-wave speed in the PMMA matrix and $\mu^{(m)} = C_{66}^{(m)}$ in the adopted isotropic local-frame constitutive description. The agreement confirms that the source-driven effective operator recovers the free-wave dispersion of the composite.

Fig. 3 presents selected effective components evaluated on the first recovered branch along the path -X–Γ–X. Primes and double primes denote real and imaginary parts, respectively. In these computations, the selected direct couplings $\tilde{\boldsymbol{\rho}}$, $\tilde{\mathbf{A}}$, and $\tilde{\mathbf{C}}$, together with the natural piezoelectric cross-coupling $\tilde{\mathbf{B}}$, satisfy the reciprocity and energy conservation identities [32]

$$\begin{aligned} \tilde{\rho}^*_{ji}(\omega,\boldsymbol{\kappa}) &= \tilde{\rho}_{ij}(\omega,\boldsymbol{\kappa}) = \tilde{\rho}_{ji}(\omega,-\boldsymbol{\kappa}), \quad & \tilde{A}^*_{ji}(\omega,\boldsymbol{\kappa}) &= \tilde{A}_{ij}(\omega,\boldsymbol{\kappa}) = \tilde{A}_{ji}(\omega,-\boldsymbol{\kappa}), \\ \tilde{B}^*_{iJ}(\omega,\boldsymbol{\kappa}) &= \tilde{B}^\dagger_{Ji}(\omega,\boldsymbol{\kappa}) = \tilde{B}_{iJ}(\omega,-\boldsymbol{\kappa}), \quad & \tilde{C}^*_{JI}(\omega,\boldsymbol{\kappa}) &= \tilde{C}_{IJ}(\omega,\boldsymbol{\kappa}) = \tilde{C}_{JI}(\omega,-\boldsymbol{\kappa}). \end{aligned} \tag{34}$$

These identities appear in the plots as the expected evenness of diagonal direct components and as the corresponding wavevector-reversal relation between adjoint pairs.

For the circular inclusion, the Willis and electromomentum couplings vanish at Γ, as expected for a geometrically inversion-symmetric unit cell in the local limit. Their real parts become nonzero for $\boldsymbol{\kappa} \neq \mathbf{0}$, reflecting spatially nonlocal, mesoscale phase effects. This interpretation is analogous to the electromagnetic homogenization results of Alù [59], where weak spatial dispersion at the lattice scale

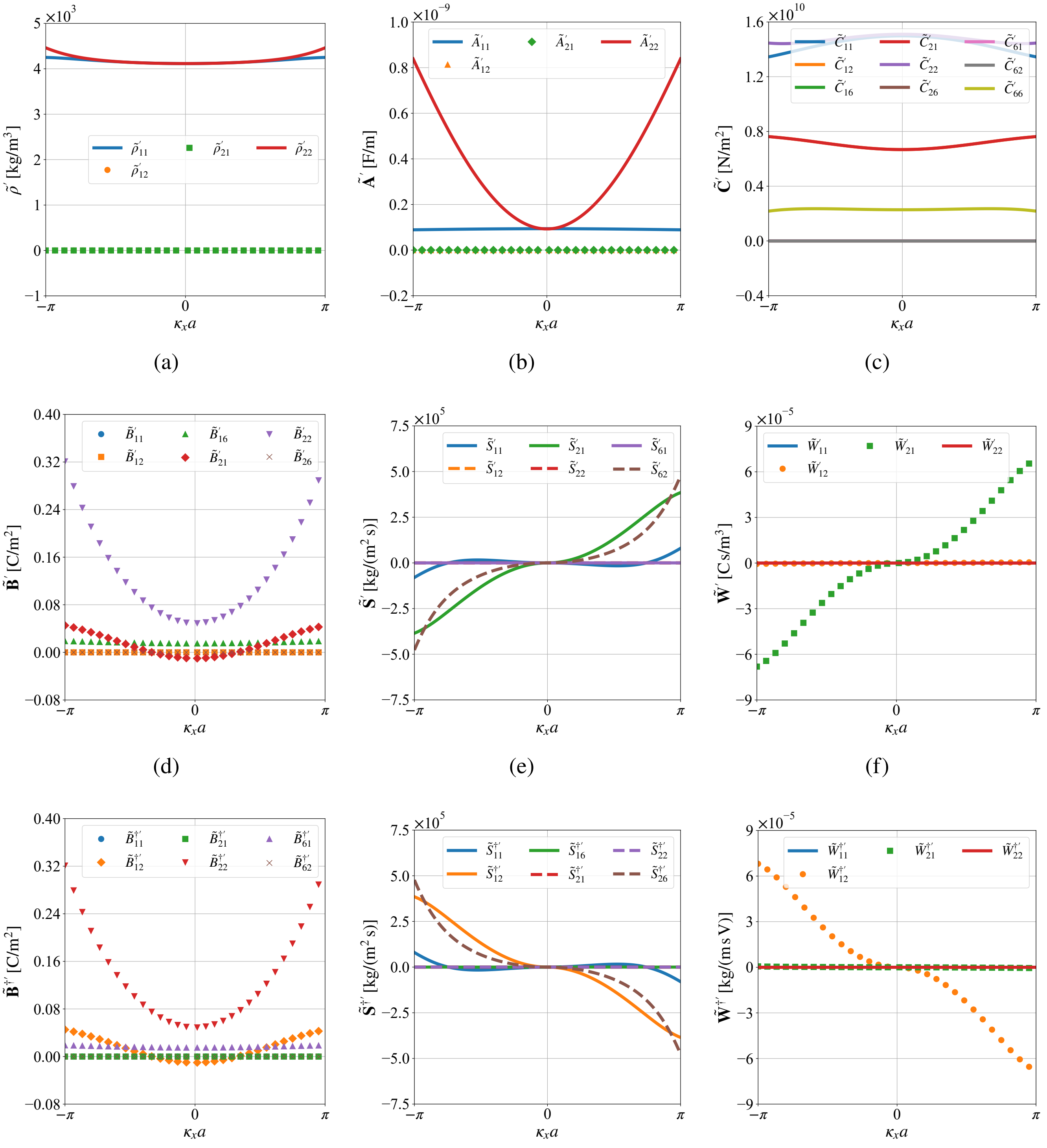

(a) (b) (c)

(d) (e) (f)

(g) (h) (i)

Figure 3: Selected real parts of the effective tensors for the circular inclusion, evaluated on the first recovered branch along $-X$–Γ–X. The inversion-symmetric geometry suppresses local Willis and electromomentum couplings at Γ, while spatial nonlocality permits finite coupling away from the zone center.

produces effective bianisotropic couplings even for centrosymmetric inclusions.

We next repeat the analysis for the circular-sector inclusion. Fig. 4 shows that the homogenized model

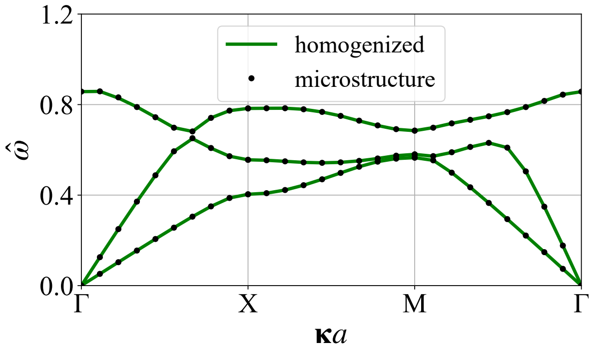

Figure 4: Bloch dispersion of the circular-sector composite along Γ–X–M–Γ. Symbols denote the spectrum of the underlying microstructure, and solid curves denote the branches recovered from the homogenized operator.

again recovers the Bloch dispersion of the underlying composite. Figs. 5 and 6 show selected real and imaginary parts of the effective tensors evaluated on the first recovered branch along -X–Γ–X. The same reciprocity and losslessness identities are satisfied, but the tensor structure is richer than in the circular cell. In addition to mesoscale nonlocal contributions away from Γ, the broken inversion symmetry of the sector cell generates Willis and electromomentum components associated with the local long-wavelength response. Thus, the two geometries distinguish two mechanisms: spatial nonlocality, which can generate mesoscale coupling even in an inversion-symmetric cell, and broken inversion symmetry, which generates additional local coupling components.

4.2 Physical violation of equivalent models

We recall that once the sources and particularly the eigenstrain are removed from the problem statement, the effective kinematic fields are no longer algebraically independent. This non-uniqueness permits the construction of source-free equivalent properties, with the electromomentum coupling suppressed, that reproduce the same dispersion surfaces. However, dispersion matching alone does not establish the physical admissibility of the homogenized model [29, 34, 61]. In electromagnetic metamaterials, Alù showed that a source-free equivalent description can reproduce wave quantities such as the dispersion relation and impedance while absorbing lattice-induced magnetoelectric coupling into effective permittivity and permeability [59, 61]. Sieck et al. [29] reached a similar conclusion for acoustic Willis media. We demonstrate next that, in the present in-plane homogenization problem, suppressing the electromomentum coupling may preserve the free-wave dispersion surfaces, only by erroneously lumping its effect into the direct couplings. The resulting equivalent description may violate the physical restrictions expected of a reciprocal lossless constitutive model, in agreement with the conclusions reached for the one-dimensional [33] and antiplane cases [34].

To show this, we start from the electric constitutive relation

$$\langle \mathbf{D} \rangle = \tilde{\mathbf{B}} \langle \nabla_s \mathbf{u} \rangle - \tilde{\mathbf{A}} \langle \nabla \phi \rangle + \tilde{\mathbf{W}} \langle \dot{\mathbf{u}} \rangle. \tag{35}$$

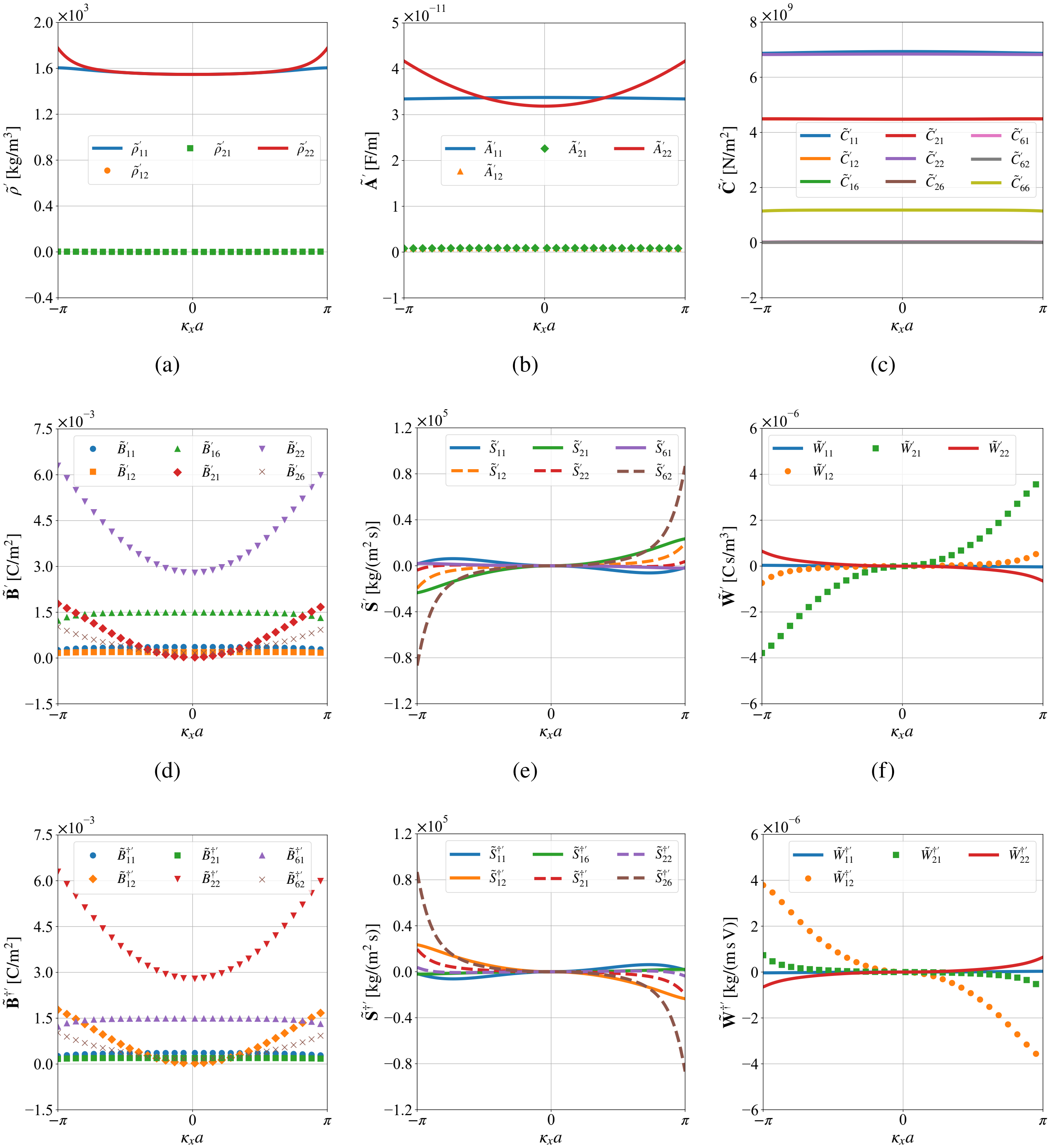

(a) (b) (c)

(d) (e) (f)

(g) (h) (i)

Figure 5: Selected real parts of the effective tensors for the circular-sector inclusion, evaluated on the first recovered branch along -X–Γ–X. The broken inversion symmetry enriches the admissible Willis and electromomentum tensor structure relative to the circular cell.

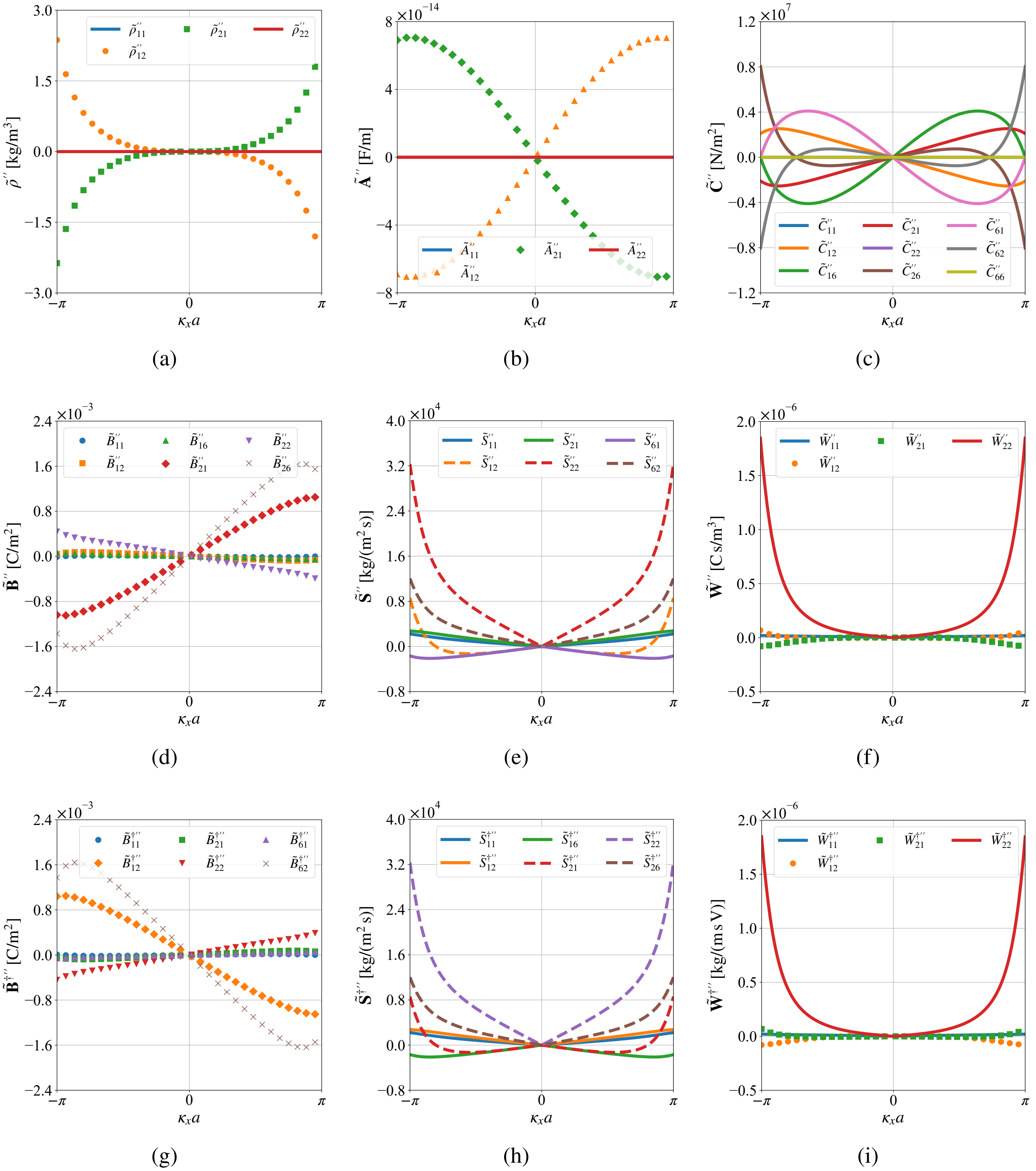

(a) (b) (c)

(d) (e) (f)

(g) (h) (i)

Figure 6: Selected imaginary parts of the effective tensors for the circular-sector inclusion, evaluated on the first recovered branch along -X–Γ–X. The nonzero components reflect the additional symmetry-allowed coupling structure introduced by the asymmetric unit cell.

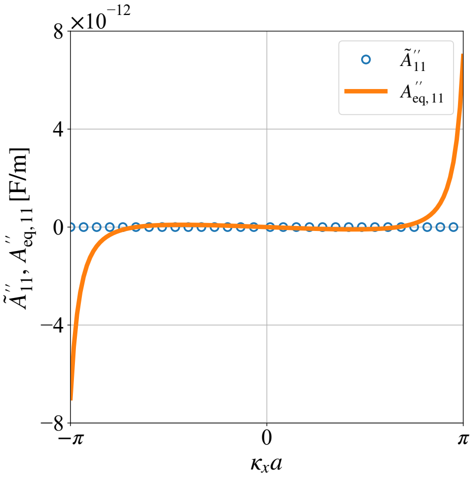

Figure 7: Imaginary part of a representative dielectric component for the source-driven homogenized model and for the corresponding equivalent model without explicit electromomentum coupling, evaluated for the circular-sector inclusion along -X–Γ–X. The equivalent description reproduces the free-wave relation but generates a dielectric response that violates the lossless reality condition satisfied by the source-driven effective dielectric tensor.

We then define an equivalent relation in which the explicit electromomentum block is suppressed,

$$\langle \mathbf{D} \rangle = \mathbf{B}_{\mathrm{eq}} \langle \nabla_{\mathrm{s}} \mathbf{u} \rangle - \mathbf{A}_{\mathrm{eq}} \langle \nabla \phi \rangle, \qquad \mathbf{B}_{\mathrm{eq}} := \tilde{\mathbf{B}}, \tag{36}$$

so that

$$\mathbf{A}_{\mathrm{eq}} \langle \nabla \phi \rangle = \tilde{\mathbf{A}} \langle \nabla \phi \rangle - \tilde{\mathbf{W}} \langle \dot{\mathbf{u}} \rangle, \tag{37}$$

and in index notation we define

$$(A_{\mathrm{eq}})_{ij} = \tilde{A}_{ij} - \frac{\left(\tilde{W}_{i1}\langle \dot{u}_1 \rangle + \tilde{W}_{i2}\langle \dot{u}_2 \rangle\right)\langle \phi_{,j} \rangle}{\langle \phi_{,1} \rangle^2 + \langle \phi_{,2} \rangle^2}. \tag{38}$$

Fig. 7 compares the source-driven component $\tilde{A}_{11}$ with the equivalent component $(A_{\mathrm{eq}})_{11}$, evaluated for the circular-sector inclusion along -X–Γ–X. The source-driven component satisfies the lossless reality condition implied by Eq. (34); By contrast, the equivalent component develops a nonzero imaginary part. This illustrates why dispersion recovery alone is not a sufficient validation criterion for the physically admissible homogenized models. This result is consistent with the demonstrations of Pernas-Salomón et al. [33] and Muhafra et al. [34], who identified equivalent descriptions that recover selected measurable wave quantities and nevertheless violate conditions required of reciprocal lossless effective descriptions.

4.3 Spatially local effective properties

In the long-wavelength regime, the macroscopic wavelength is large compared with the unit cell size a, so that $|\boldsymbol{\kappa}|a \ll 1$. In this regime, spatial nonlocality is weak and the effective response can be approximated by local, frequency-dependent tensors. In the present plane-wave formulation, this local limit is obtained by evaluating the operator at $\boldsymbol{\kappa} = \mathbf{0}$, equivalently by replacing $\boldsymbol{\kappa} + \mathbf{G}$ with $\mathbf{G}$ in the Fourier-domain differential operators. Fig. 8 shows selected components of these local tensors for the circular-sector inclusion as functions of the normalized frequency. We observe that the direct couplings satisfy the conditions

$$\frac{\partial}{\partial\omega}\operatorname{Re}\tilde{\rho}_{(i)(i)} \geq 0, \quad \frac{\partial}{\partial\omega}\operatorname{Re}\tilde{A}_{(i)(i)} \geq 0, \quad \frac{\partial}{\partial\omega}\operatorname{Re}\tilde{C}_{(I)(I)} \leq 0 \quad \text{(no summation)}, \tag{39}$$

that follow from passivity together with differentiation of the Kramers–Kronig causality relations [32, 61, 62].

4.4 Homogenization at arbitrary wavevector–frequency pairs

In the source-driven formulation, the driving frequency and wavevector are prescribed independently. The resulting effective operator can therefore be evaluated at arbitrary frequency–wavevector pairs, including pairs that do not lie on the dispersion surfaces. To illustrate this capability, we fix the representative wavevector $\kappa_1 = \pi/a$, $\kappa_2 = 0$, and compute the effective properties of the circular-sector composite as functions of $\hat{\omega}$. Figs. 9–10 show the real and imaginary parts,respectively, of selected off-dispersion effective properties. The separation into real and imaginary plots highlights that the imaginary components are negligible over the examined frequency range, while the finite Willis and electromomentum components encode the nonlocal dynamic coupling of the homogenized medium. Compared with the on-branch effective properties, the apparent resonance locations generally shift, and the coupling tensors may acquire nonzero imaginary parts even when the standard blocks remain predominantly real. Throughout these off-dispersion calculations, the reciprocity identities remain satisfied, as expected for composites made of reciprocal constituents.

4.5 Canonical half-space scattering validation

Interface scattering tests have been used in dynamic homogenization as a quantitative measure of whether a periodic medium can be replaced by its homogenized counterpart in finite configurations [63–65]. We therefore conclude our numerical analysis by examining whether the local effective medium reproduces the scattering response of the underlying composite in a canonical interface scattering problem [65], simulated using finite elements.

The computational setup excites a narrowband oblique shear wave incident from a homogeneous PMMA incident medium onto either the circular-sector composite or its corresponding local effective medium. The comparison is a long-wavelength, center-frequency test of the local homogenized model.

The material region in which the composite is replaced by the effective medium contains two unit-cell periods in the propagation direction x_1 and five periods in the transverse direction x_2. The full right-side computational domain is longer because it also contains a propagation buffer, made of the same right-side

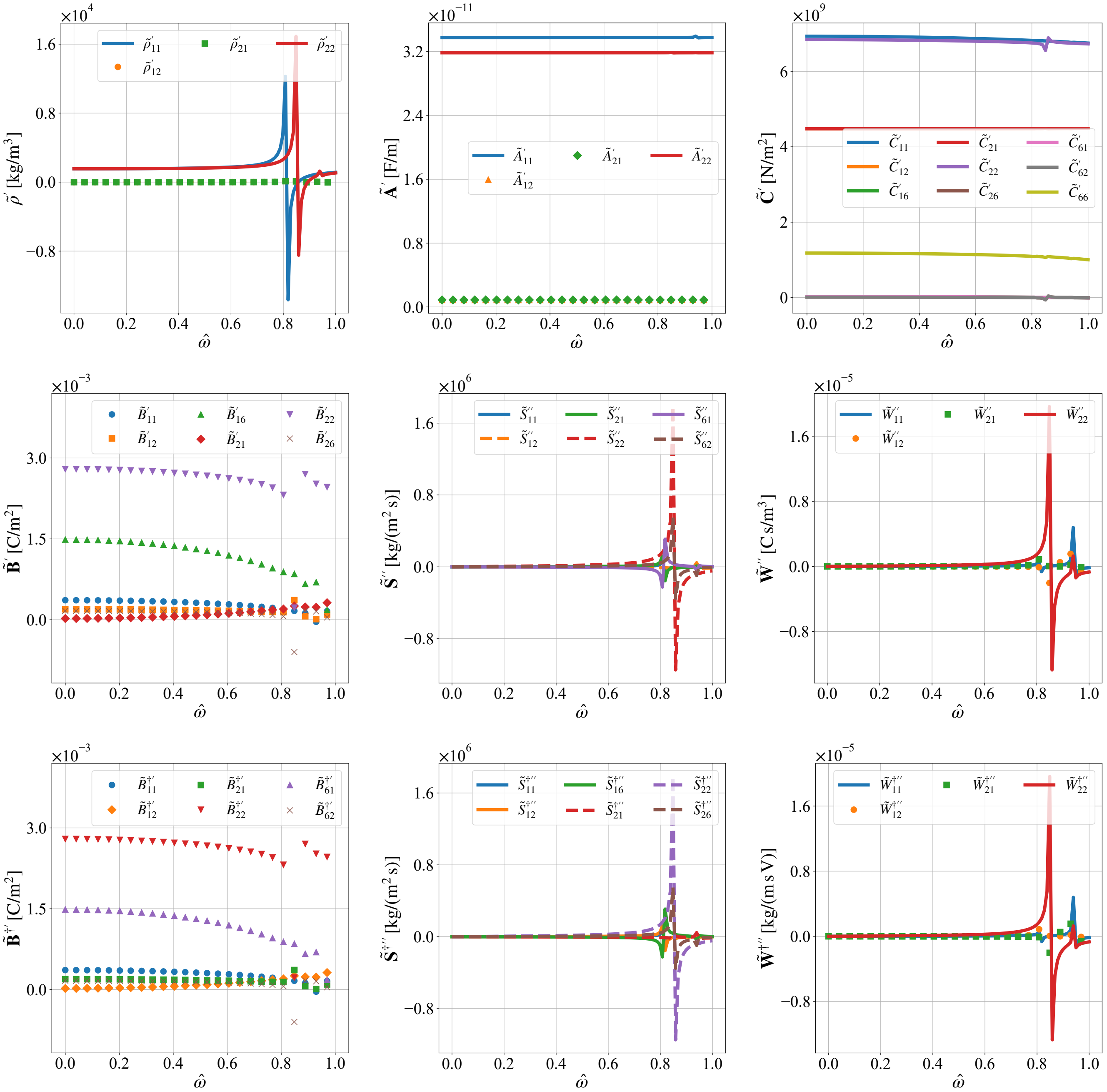

Figure 8: Selected components of the local effective tensors of the circular-sector composite as functions of the normalized frequency $\hat{\omega}$.

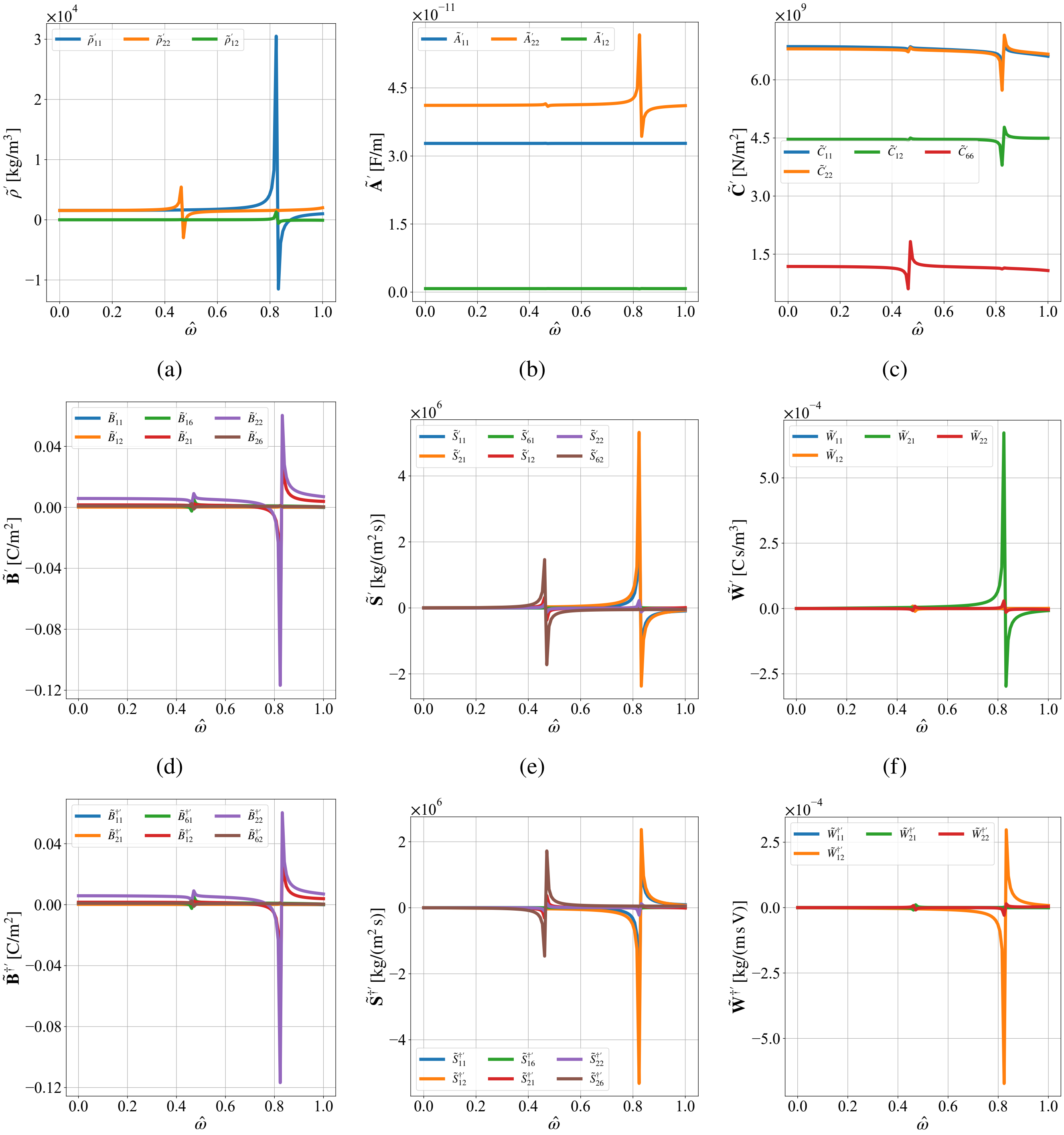

(a) (b) (c)

(d) (e) (f)

(g) (h) (i)

Figure 9: Selected real parts of the effective tensors of the circular-sector composite at the fixed off-dispersion wavevector $\kappa_1 = \pi/a$, $\kappa_2 = 0$, plotted as functions of the normalized frequency $\hat{\omega}$.

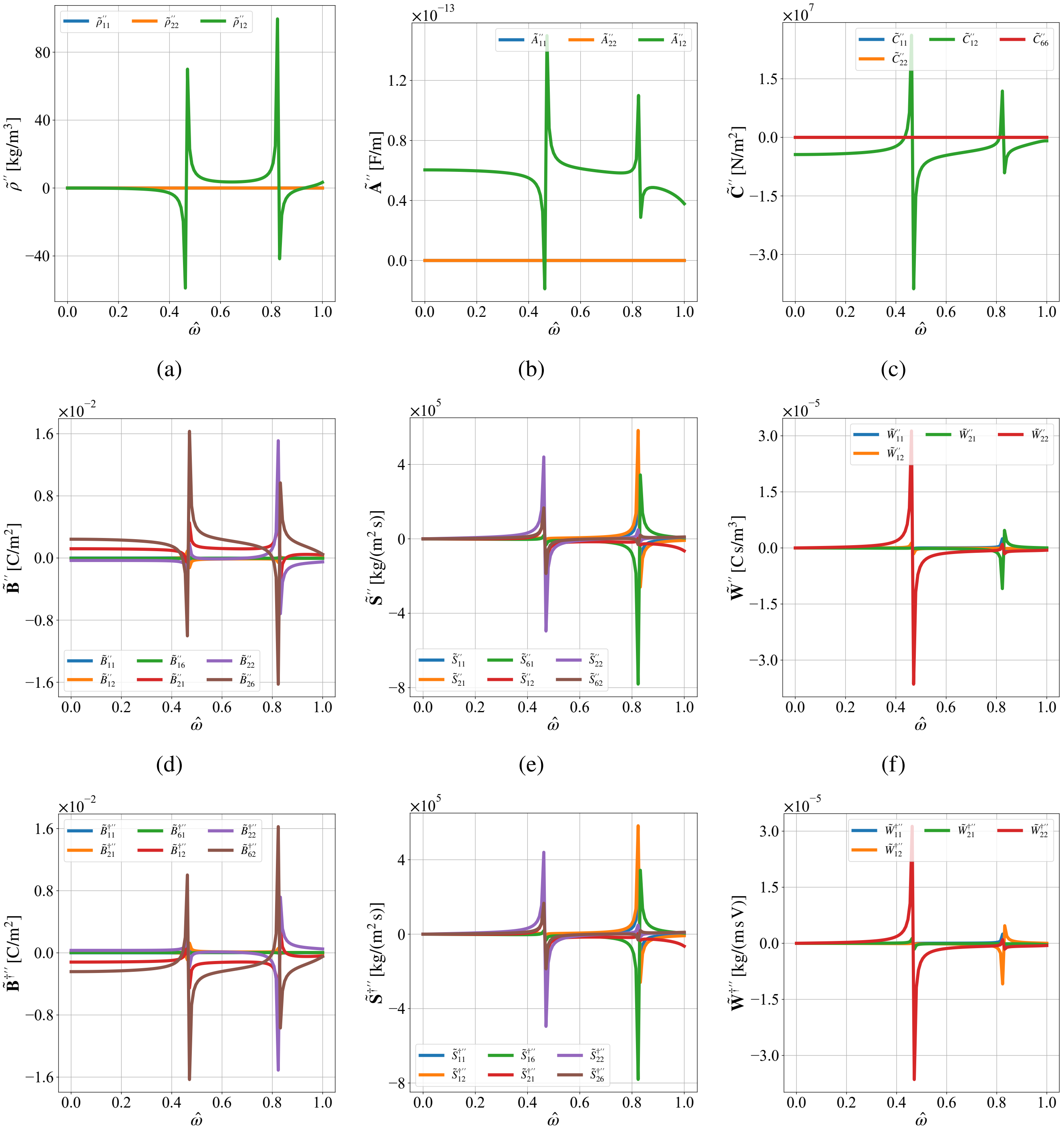

(a) (b) (c)

(d) (e) (f)

(g) (h) (i)

Figure 10: Selected imaginary parts of the effective tensors of the circular-sector composite at the fixed off-dispersion wavevector $\kappa_1 = \pi/a$, $\kappa_2 = 0$, plotted as functions of the normalized frequency $\hat{\omega}$.

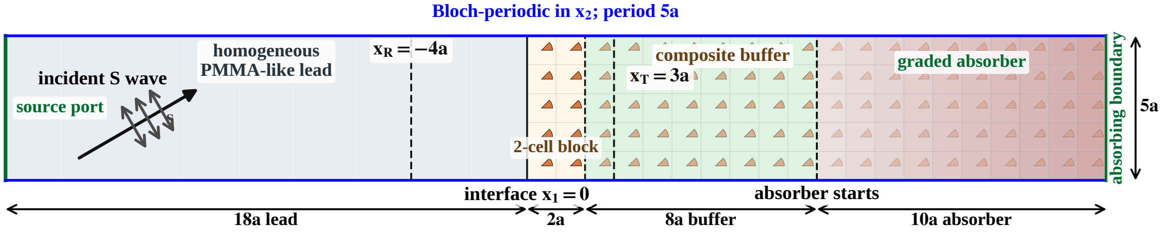

Figure 11: Computational layout for the canonical scattering problem.

medium, followed by a graded absorbing region.[2] This layout is illustrated in Fig. 11. The effective-medium calculation uses the same incident medium, buffer, absorber, final time, and monitor positions as the composite calculation; only the right-side material model is changed.

The incidence angle is imposed by prescribing the transverse wavenumber $\kappa_2 = k_s^{(m)} \sin\theta$, where $k_s^{(m)} = 2\pi/\lambda_0$ is the shear wavenumber in the homogeneous PMMA incident medium at the pulse center frequency. The finite-element unknowns are Bloch-envelope fields that are periodic in x_2; the corresponding real physical fields are reconstructed from these envelopes as detailed in Appendix B. Electrically, the simulations are open-circuit: ϕ is the electric-potential envelope, continuity of the normal electric displacement is enforced weakly across material interfaces, and the external electrical boundary condition is $\mathbf{D} \cdot \mathbf{n} = 0$, where $\mathbf{n}$ is the outward unit normal and $\mathbf{D}$ is the electric-displacement envelope.[3]

The incident wave is applied by a modal impedance source on the left boundary of the homogeneous PMMA incident medium. For the prescribed κ_2, this source injects the incoming shear wave and absorbs waves reflected back toward the source. The far-right boundary is placed behind the graded absorber, so outgoing waves are attenuated before reaching the outer mechanical boundary. We simulate three cases. Case 1 has $\theta = 30°$ and $\lambda_0 = 20a$, where θ is measured counterclockwise from x_1 and λ_0 is the incident shear wavelength in the PMMA medium, corresponding to $\hat{\omega} = 0.05$. Case 2 has $\theta = 15°$ and $\lambda_0 = 20a$. Case 3 has $\theta = 30°$ and $\lambda_0 = 50a$, corresponding to $\hat{\omega} = 0.02$; for this case, the local effective tensors are recomputed at $\hat{\omega} = 0.02$.

We calculate the reflection and transmission coefficients, defined as the energy ratios

$$R = \frac{E_{\text{ref}}}{E_{\text{inc}}}, \qquad T = \frac{E_{\text{tr,region}}}{E_{\text{inc}}}, \tag{40}$$

where E_{inc} is the incident energy measured in a homogeneous reference run, E_{ref} is the reflected energy returning through the incident medium, and $E_{\text{tr,region}}$ is the energy that has entered the right-side region by the final time (detailed finite-element energy definitions and diagnostics are given in Appendix B).

---

[2] Cases 1 and 2 use 2 + 8 + 10 = 20 periods on the right side: two periods in the material region being compared, eight additional periods used as a propagation buffer, and ten periods in the graded absorber. Case 3 uses 2 + 12 + 20 = 34 periods to accommodate the longer pulse.

[3] One electric-potential degree of freedom is fixed only to remove the constant-potential gauge.

Table 2: Reflection and transmission coefficient extracted from the Long-wavelength canonical scattering simulations. Cases 1 and 2 use $\lambda_0 = 20a$ ($\hat{\omega} = 0.05$), while Case 3 uses $\lambda_0 = 50a$ ($\hat{\omega} = 0.02$).

Case	θ	Model	R	T	$R+T$
Case 1	30°	Composite	0.0325	0.9393	0.9719
		Effective electromomentum medium	0.0316	0.9335	0.9652
Case 2	15°	Composite	0.0127	0.9598	0.9726
		Effective electromomentum medium	0.0126	0.9570	0.9696
Case 3	30°	Composite	0.0222	0.9657	0.9879
		Effective electromomentum medium	0.0224	0.9646	0.9870

Specifically,

$$E_{\text{tr,region}} = E_{\text{absorbed,right}}(t_{\text{end}}) + E_{\text{stored,right}}(t_{\text{end}}), \tag{41}$$

where $E_{\text{absorbed,right}}$ is the energy dissipated in the right absorbing layer and $E_{\text{stored,right}}$ is the remaining kinetic plus internal energy in the right-side computational region. This definition is less sensitive to cell-scale oscillations in the heterogeneous region than a single transmitted-flux cut. Since the diagnostics are finite-time measurements, $R+T$ is not forced to equal unity exactly; the deviation is attributed mainly to residual energy remaining in the computational domain at t_{end}.

The results in Table 2 show that the homogenized medium reproduces the reflected and transmitted energies of the underlying composite. In Cases 1 and 2, the reflected coefficients agree closely and the transmitted energies differ only slightly. The agreement is strongest in Case 3, where the longer wavelength further suppresses cell-scale scattering. This trend is consistent with the expected improvement of a local homogenized approximation as the imposed wavelength becomes large relative to the unit cell.

The displacement snapshots are generated from saved finite-element envelope states and show the real physical displacement projected onto the incident shear wave polarization, as defined in Appendix B. The flux snapshots show the corresponding cycle-averaged x_1-directed power-flux density used in the scattering diagnostics.

The displacement snapshots in Figs. 12–14 illustrate the expected distinction between the two descriptions. The composite exhibits local oscillations associated with the PMMA/PZT–4 contrast, whereas the homogeneous effective medium smooths these oscillations while preserving the macroscopic wavefront, propagation direction, and energy partition. Accordingly, these snapshots should be interpreted as a comparison of the macroscopic wave response rather than as a pointwise recovery of the microscopic fields.

The complementary energy-flux snapshots in Figs. 15–17 visualize the x_1-directed energy transport used in the scattering diagnostics. These fields are intended as averaged energy-transport indicators. For the homogeneous effective-medium snapshots, the flux is evaluated from recovered nodal gradients and then cell-scale averaged to avoid imprinting the microstructure-conforming mesh on an otherwise homogeneous field; the tabulated values of R and T, however, are obtained from the unsmoothed monitor-

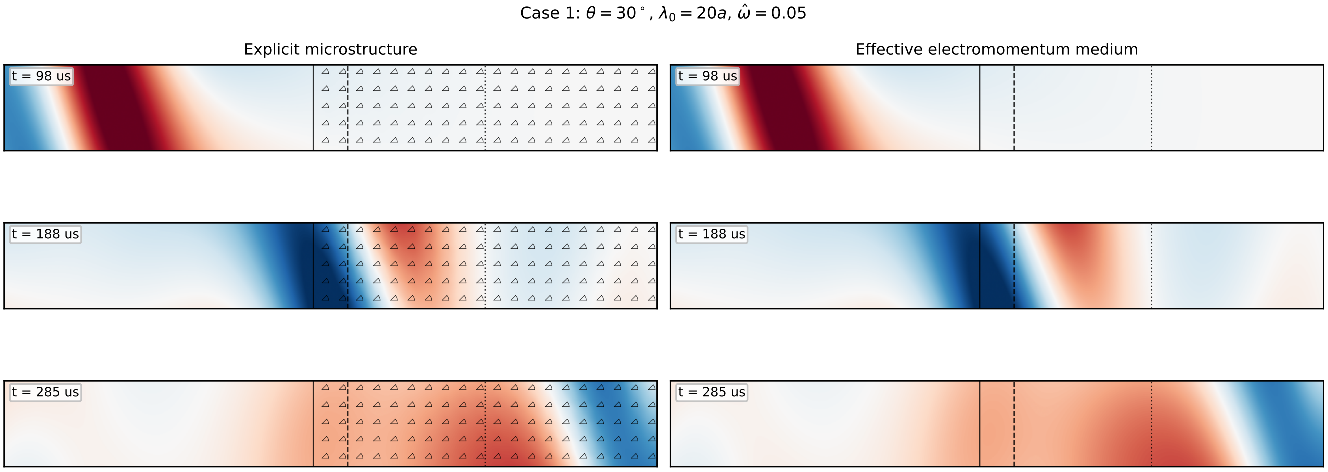

Figure 12: Time-domain displacement snapshots for Case 1 in Table 2, with $\lambda_0 = 20a$, and $\theta = 30°$. The plotted scalar field is the real physical displacement projected onto the incident S-wave polarization. This signed projection preserves phase and isolates the directly excited shear component, avoiding the P/S mixing and loss of sign that would occur in a displacement-magnitude plot.

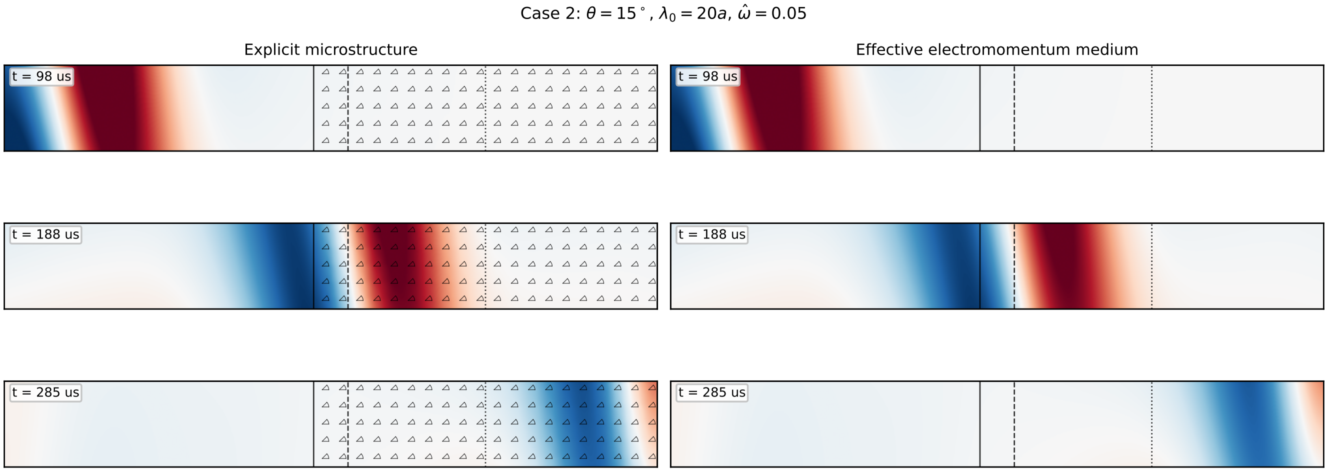

Figure 13: Time-domain displacement snapshots for Case 2 in Table 2, with $\lambda_0 = 20a$, and $\theta = 15°$. The plotted scalar field is the signed displacement component along the incident S-wave polarization. This projection preserves the wave phase and makes the explicit and effective shear-polarized wavefronts directly comparable.

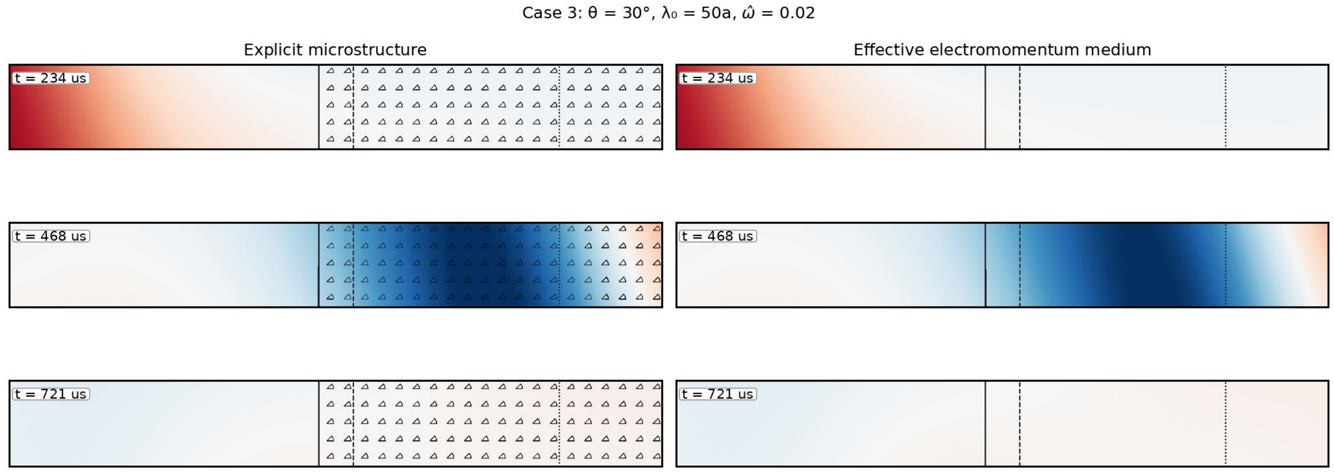

Figure 14: Time-domain displacement snapshots for Case 3 in Table 2, with $\lambda_0 = 50a$, $\theta = 30°$, and effective tensors recomputed at $\hat{\omega} = 0.02$. The plotted scalar field is the signed displacement component along the incident S-wave polarization. This phase-resolved shear component highlights the longer-wavelength macroscopic wavefront while avoiding magnitude-only loss of phase.

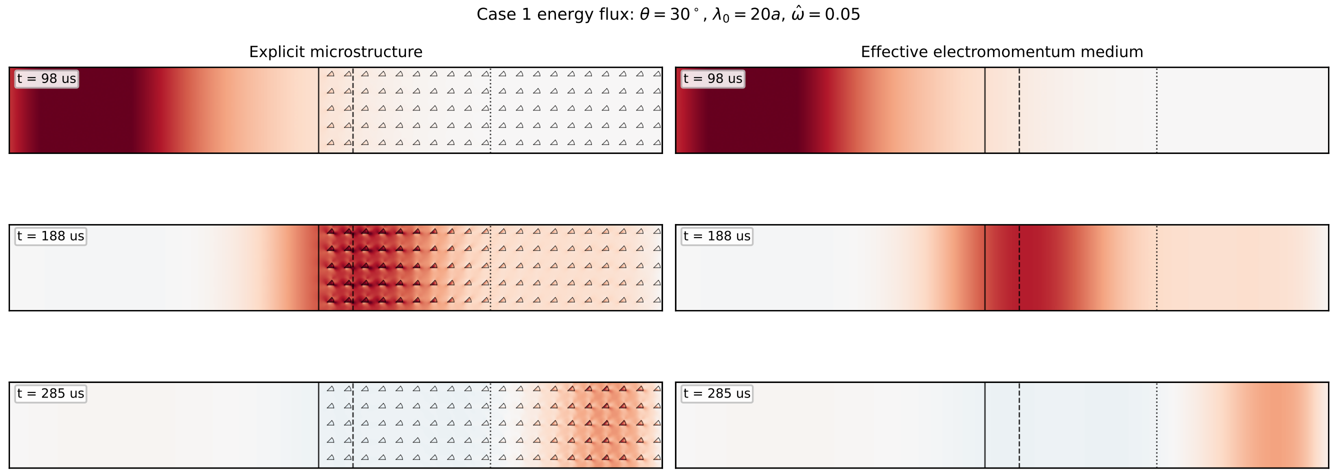

Figure 15: x_1-directed energy-flux-density snapshots for Case 1 in Table 2. The plotted scalar is the cycle-averaged envelope power-flux density q_1, positive for energy flow toward the transmitted side. These panels complement the displacement snapshots by showing the energy-transport path integrated over monitor cuts to obtain the scattering diagnostics.

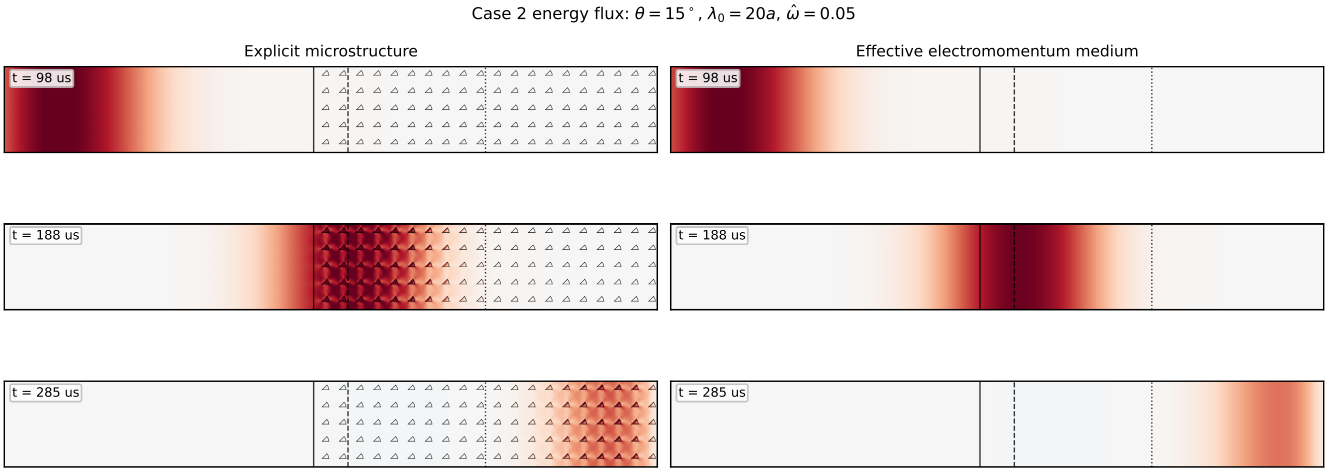

Figure 16: x_1-directed energy-flux-density snapshots for Case 2 in Table 2. The plotted scalar is the cycle-averaged envelope power-flux density q_1, positive toward $+x_1$. The flux field shows where the transmitted energy is carried through the explicit and homogenized regions, while the quantitative comparison is given by the integrated R and T values.

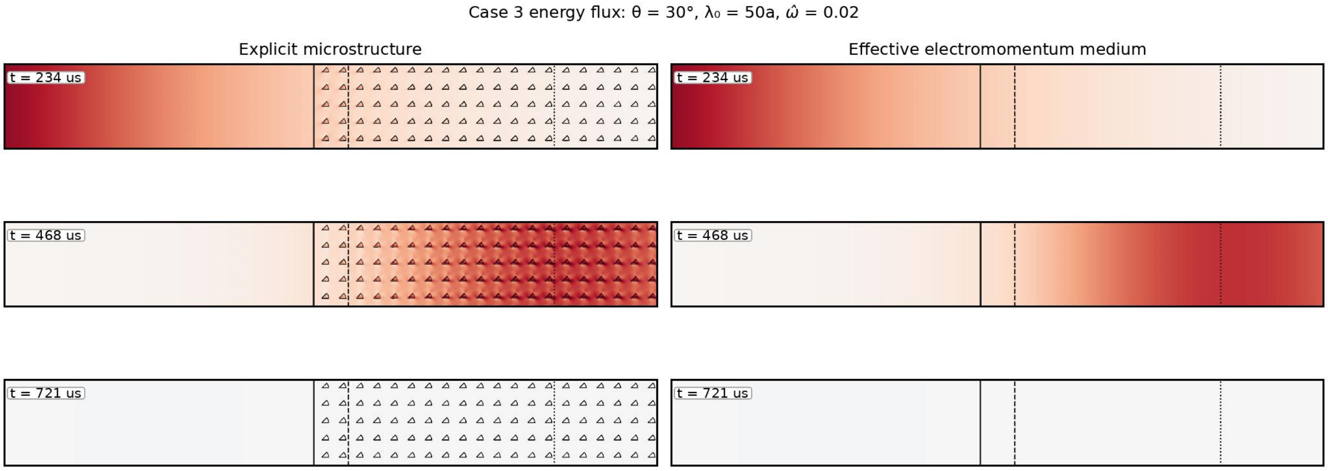

Figure 17: x_1-directed energy-flux-density snapshots for Case 3 in Table 2. The plotted scalar is the cycle-averaged envelope power-flux density q_1, with positive values directed toward the transmitted side. At the lower normalized frequency, the explicit and effective flux distributions show the same large-scale energy-transport path.

flux integration.

This comparison validates the long-wavelength averaged scattering response for the chosen interface truncation, incidence angles, and narrowband excitations. It should not be interpreted as pointwise recovery of the local microscopic fields, nor as an interface-independent validation at arbitrary wavelength. Within the present long-wavelength regime, the local effective medium captures the macroscopic reflection, transmission, and energy-transport behavior of the explicit sector-inclusion composite.

5 Concluding remarks and outlook

The theoretical discovery of electromomentum coupling established that piezoelectric composites can exhibit macroscopic interactions between electric and dynamic fields that are absent in their constituents [31]. Most subsequent works have investigated this effect in settings where the primary mechanical field is scalar [33, 34, 36, 38, 41, 42, 44–47, 66], while the tensorial in-plane problem, in which two wave polarizations coexist, has remained less explored [42]. Here, we developed and applied a source-driven dynamic homogenization scheme to determine the effective properties of periodic piezoelectric composites subjected to such in-plane excitations.

The formulation follows the central ideas of Willis' homogenization theory and its extension to piezoelectric media by Pernas-Salomón and Shmuel [20, 31]. The macroscopic fields are defined by ensemble averaging, which reduces in the periodic case to averaging the periodic part of the Bloch fields over the unit cell. The microscopic problem accounts for driving eigenstrain, body force, and free-charge sources, so that the effective kinematic fields are independent and the effective operator is uniquely determined for prescribed driving frequencies and wavevectors, not only on the dispersion surfaces. The Bloch-periodic fields and material properties are then expanded in plane waves, and the fluctuating Fourier coefficients are eliminated to obtain the effective relation between the averaged kinetic and kinematic fields. Our numerical examples demonstrate several features. First, the homogenized model recovers the Bloch dispersion of the underlying composites. Second, the computed effective tensors satisfy the expected restrictions associated with reciprocity, losslessness, and causality. This supports the physical admissibility of the source-driven constitutive description, whereas source-free equivalent descriptions that suppress explicit electromomentum coupling may violate these restrictions [32–34, 57, 61, 67]. Third, by comparing circular and circular-sector inclusions, we distinguished two physical mechanisms. The circular, geometrically centrosymmetric cell exhibits Willis and electromomentum couplings beyond the long-wavelength limit, associated with mesoscale phase effects and spatial nonlocality. The asymmetric sector cell, by contrast, generates a richer set of coupling components, including contributions that persist in the local long-wavelength response.

We also tested the local effective medium in a long-wavelength canonical scattering problem [63, 65]. The comparison between the response of the underlying composite and its homogenized replacement shows good agreement in reflected and transmitted energy for the incidence angles and wavelengths considered. The underlying composite retains cell-scale oscillations, whereas the effective medium smooths these fluctuations while preserving the macroscopic wavelength, propagation direction, and energy partition. This calculation should be interpreted as a validation of the averaged long-wavelength scattering response for the chosen interface and excitation, rather than as pointwise recovery of the microscopic fields or as an interface-independent statement at arbitrary wavelength.

Collectively, this work addresses a missing step in the analysis of the electromomentum coupling in the in-plane tensorial setting, providing a tangible route for calculating in-plane electromomentum tensors and evaluating their properties. In future work, we will extend the framework to fully three-dimensional periodic piezoelectric composites and subsequently derive reduced beam and plate theories that inherit electromomentum coupling from the underlying three-dimensional medium. These developments will connect source-driven homogenization with finite-domain simulations and experimental characterization, supporting future designs for elastic-wave control applications based on electromomentum coupling.

Acknowledgments

GS dedicates this work to his dear wife, Yana Shmuel, and their beloved first born, Liam Shmuel. GS acknowledges funding by the U.S. MURI project W911NF-25-2-0176 and by the European Union (ERC, EXCEPTIONAL, Project No. 101045494). Funded by the European Union. The views and opinions expressed are those of the author(s) only and do not necessarily reflect those of the European Union or the European Research Council Executive Agency. Neither the European Union nor the granting authority can be held responsible for them

A Dispersion relation of the homogenized medium

For completeness, we derive the dispersion relation associated with the homogenized model. The derivation follows the same general strategy as in the antiplane case [34]: we substitute an averaged Bloch form into the effective constitutive equations, insert the result into the macroscopic balance laws, and eliminate the electric-potential amplitude to obtain a closed compatibility equation for the averaged displacement.

For free waves we set

$$\mathbf{f} = \mathbf{0}, \qquad q = 0, \qquad \boldsymbol{\eta} = \mathbf{0}, \tag{A1}$$

and seek averaged fields of the form

$$\langle \zeta \rangle(\mathbf{x}, t) = \bar{\zeta}\, e^{\,i(\boldsymbol{\kappa}\cdot\mathbf{x}-\omega t)}. \tag{A2}$$

We define

$$\mathsf{\bar{u}} = \begin{pmatrix} \bar{u}_1 \\ \bar{u}_2 \end{pmatrix}, \qquad \mathsf{k} := \begin{pmatrix} \kappa_1 \\ \kappa_2 \end{pmatrix}. \tag{A3}$$

The averaged strain amplitude is obtained from

$$\langle \nabla_{\mathrm{s}} \mathbf{u} \rangle = i\, \mathsf{R}(\boldsymbol{\kappa})\, \mathsf{\bar{u}}\, e^{i(\boldsymbol{\kappa}\cdot\mathbf{x}-\omega t)}, \qquad \mathsf{R}(\boldsymbol{\kappa}) := \begin{pmatrix} \kappa_1 & 0 \\ 0 & \kappa_2 \\ \kappa_2 & \kappa_1 \end{pmatrix}. \tag{A4}$$

Using the effective constitutive relations, the averaged kinetic amplitudes are

$$\begin{aligned} \bar{\boldsymbol{\sigma}} &= i\, \tilde{\mathsf{C}}\, \mathsf{R}\, \mathsf{\bar{u}} + i\, \tilde{\mathsf{B}}^{\dagger}\, \mathsf{k}\, \bar{\phi} - i\omega\, \tilde{\mathsf{S}}\, \mathsf{\bar{u}}, \\ \bar{\mathsf{D}} &= i\, \tilde{\mathsf{B}}\, \mathsf{R}\, \mathsf{\bar{u}} - i\, \tilde{\mathsf{A}}\, \mathsf{k}\, \bar{\phi} - i\omega\, \tilde{\mathsf{W}}\, \mathsf{\bar{u}}, \\ \bar{\mathsf{p}} &= i\, \tilde{\mathsf{S}}^{\dagger}\, \mathsf{R}\, \mathsf{\bar{u}} + i\, \tilde{\mathsf{W}}^{\dagger}\, \mathsf{k}\, \bar{\phi} - i\omega\, \tilde{\boldsymbol{\rho}}\, \mathsf{\bar{u}}, \end{aligned} \tag{A5}$$

where

$$\tilde{\mathsf{C}} \in \mathbb{C}^{3\times3}, \quad \tilde{\mathsf{B}} \in \mathbb{C}^{2\times3}, \quad \tilde{\mathsf{A}} \in \mathbb{C}^{2\times2}, \quad \tilde{\mathsf{S}} \in \mathbb{C}^{3\times2}, \quad \tilde{\mathsf{W}} \in \mathbb{C}^{2\times2}, \quad \tilde{\boldsymbol{\rho}} \in \mathbb{C}^{2\times2}. \tag{A6}$$

The source-free macroscopic balance laws are

$$\nabla \cdot \langle \boldsymbol{\sigma} \rangle = \langle \dot{\mathbf{p}} \rangle, \qquad \nabla \cdot \langle \mathbf{D} \rangle = 0. \tag{A7}$$

After Bloch reduction, these become

$$i\, \mathsf{R}(\boldsymbol{\kappa})^{\mathsf{T}} \bar{\boldsymbol{\sigma}} + i\omega\, \bar{\mathsf{p}} = 0, \qquad i\, \mathsf{k}^{\mathsf{T}} \bar{\mathsf{D}} = 0. \tag{A8}$$

Substituting Eq. (A5) into Eq. (A8) gives a homogeneous algebraic system for $(\mathsf{\bar{u}}, \bar{\phi})$,

$$\begin{pmatrix} \mathsf{K}_{uu}(\omega,\boldsymbol{\kappa}) & \mathsf{K}_{u\phi}(\omega,\boldsymbol{\kappa}) \\ \mathsf{K}_{\phi u}(\omega,\boldsymbol{\kappa}) & K_{\phi\phi}(\omega,\boldsymbol{\kappa}) \end{pmatrix} \begin{pmatrix} \mathsf{\bar{u}} \\ \bar{\phi} \end{pmatrix} = \begin{pmatrix} 0 \\ 0 \end{pmatrix}, \tag{A9}$$

where

$$\begin{aligned} \mathsf{K}_{uu}(\omega,\boldsymbol{\kappa}) &= \omega^2 \tilde{\boldsymbol{\rho}} + \omega\Big(\mathsf{R}^{\mathsf{T}}\tilde{\mathsf{S}} - \tilde{\mathsf{S}}^{\dagger}\mathsf{R}\Big) - \mathsf{R}^{\mathsf{T}}\tilde{\mathsf{C}}\mathsf{R}, \\ \mathsf{K}_{u\phi}(\omega,\boldsymbol{\kappa}) &= -\mathsf{R}^{\mathsf{T}}\tilde{\mathsf{B}}^{\dagger}\mathsf{k} - \omega\, \tilde{\mathsf{W}}^{\dagger}\mathsf{k}, \\ \mathsf{K}_{\phi u}(\omega,\boldsymbol{\kappa}) &= -\mathsf{k}^{\mathsf{T}}\tilde{\mathsf{B}}\mathsf{R} + \omega\, \mathsf{k}^{\mathsf{T}}\tilde{\mathsf{W}}, \\ K_{\phi\phi}(\omega,\boldsymbol{\kappa}) &= \mathsf{k}^{\mathsf{T}}\tilde{\mathsf{A}}\, \mathsf{k}. \end{aligned} \tag{A10}$$

All effective blocks in Eq. (A10) are evaluated at the same pair $(\omega, \boldsymbol{\kappa})$. Provided that

$$\alpha(\omega, \boldsymbol{\kappa}) := \mathsf{k}^{\mathsf{T}} \tilde{\mathsf{A}}(\omega, \boldsymbol{\kappa})\, \mathsf{k} \neq 0, \tag{A11}$$

the electric-potential amplitude can be eliminated from the second row of Eq. (A9), giving

$$\bar{\phi} = -K_{\phi\phi}^{-1} \mathsf{K}_{\phi u} \bar{\mathsf{u}} = -\alpha(\omega, \boldsymbol{\kappa})^{-1} \mathsf{K}_{\phi u} \bar{\mathsf{u}}. \tag{A12}$$

Substitution into the first row of Eq. (A9) yields a reduced equation for the averaged displacement,

$$\mathsf{K}_{\text{red}}(\omega, \boldsymbol{\kappa})\, \bar{\mathsf{u}} = 0, \qquad \mathsf{K}_{\text{red}} := \mathsf{K}_{uu} - \mathsf{K}_{u\phi}\, K_{\phi\phi}^{-1}\, \mathsf{K}_{\phi u}. \tag{A13}$$

The free-wave dispersion relation of the homogenized medium is therefore

$$\det \mathsf{K}_{\text{red}}(\omega, \boldsymbol{\kappa}) = 0. \tag{A14}$$

At points where $K_{\phi\phi} = 0$, for example at $\boldsymbol{\kappa} = \mathbf{0}$, one should use the full coupled system in Eq. (A9) or take the appropriate limiting value of Eq. (A13).

To display the explicit powers of ω, define

$$\mathsf{g}_0 := \mathsf{R}^{\mathsf{T}} \tilde{\mathsf{B}}^{\dagger} \mathsf{k}, \qquad \mathsf{g}_1 := \tilde{\mathsf{W}}^{\dagger} \mathsf{k}, \qquad \mathsf{r}_0^{\mathsf{T}} := \mathsf{k}^{\mathsf{T}} \tilde{\mathsf{B}} \mathsf{R}, \qquad \mathsf{r}_1^{\mathsf{T}} := \mathsf{k}^{\mathsf{T}} \tilde{\mathsf{W}}. \tag{A15}$$

Then

$$\mathsf{K}_{u\phi} = -(\mathsf{g}_0 + \omega \mathsf{g}_1), \qquad \mathsf{K}_{\phi u} = -(\mathsf{r}_0^{\mathsf{T}} - \omega \mathsf{r}_1^{\mathsf{T}}), \tag{A16}$$

and the reduced equation may be written as

$$\Big(\omega^2 \mathsf{P}_2(\omega, \boldsymbol{\kappa}) + \omega \mathsf{P}_1(\omega, \boldsymbol{\kappa}) + \mathsf{P}_0(\omega, \boldsymbol{\kappa})\Big) \bar{\mathsf{u}} = 0, \tag{A17}$$

with

$$\begin{aligned}
\mathsf{P}_2(\omega, \boldsymbol{\kappa}) &= \tilde{\boldsymbol{\rho}} + \alpha(\omega, \boldsymbol{\kappa})^{-1} \mathsf{g}_1 \mathsf{r}_1^{\mathsf{T}}, \\
\mathsf{P}_1(\omega, \boldsymbol{\kappa}) &= \mathsf{R}^{\mathsf{T}} \tilde{\mathsf{S}} - \tilde{\mathsf{S}}^{\dagger} \mathsf{R} + \alpha(\omega, \boldsymbol{\kappa})^{-1} \Big(\mathsf{g}_0 \mathsf{r}_1^{\mathsf{T}} - \mathsf{g}_1 \mathsf{r}_0^{\mathsf{T}}\Big), \\
\mathsf{P}_0(\omega, \boldsymbol{\kappa}) &= -\mathsf{R}^{\mathsf{T}} \tilde{\mathsf{C}} \mathsf{R} - \alpha(\omega, \boldsymbol{\kappa})^{-1} \mathsf{g}_0 \mathsf{r}_0^{\mathsf{T}}.
\end{aligned} \tag{A18}$$

Eq. (A17) is quadratic only after the effective tensors are held fixed. In the exact homogenized problem, the tensors entering P_0, P_1, and P_2 depend on $(\omega, \boldsymbol{\kappa})$, so Eq. (A14) is a nonlinear compatibility condition. In the recovery procedure used in the computations, this nonlinearity is handled locally: the tensors are evaluated at the microstructural seed frequency and at selected reciprocal-shift representatives of the wavevector, and the resulting fixed-coefficient quadratic problem is solved to recover the nearby homogenized branch.

B Finite-element scattering diagnostics

This appendix gives the finite-element definitions used in the scattering validation of Sec. 4.5. The transverse wavenumber κ_2 is prescribed by the incidence angle, and the finite-element unknowns are Bloch-envelope fields that are periodic in x_2. For any scalar mechanical or electrical envelope component s, the real physical field is reconstructed as

$$s_{\text{phys}}(x_1, x_2, t) = \Re\{s_{\text{env}}(x_1, x_2, t)e^{i\kappa_2 x_2}\}, \tag{B1}$$

where $\Re$ denotes the real part of the function. For a vertical monitor Γ, the cycle-averaged complex-envelope power $P_\Gamma(t)$, namely the power crossing that monitor at time t, is

$$P_\Gamma(t) = \int_\Gamma q_{x_1}(x_2, t)\,\mathrm{d}x_2, \qquad q_1 = -\frac{1}{2}\Re\left\{\sigma_{11}v_1^* + \sigma_{12}v_2^* + \dot{\phi}D_1^*\right\}. \tag{B2}$$

Here q_{x_1} is the x_1-directed power-flux density, $v_i = \dot{u}_i$ are the mechanical velocity envelopes, σ_{11} and σ_{12} are stress-envelope components, $\dot{\phi}$ is the electric-potential time derivative, and D_1 is the x_1-component of the electric-displacement envelope. Positive power is directed toward $+x_1$. The factor $1/2$ and the complex conjugates follow from cycle averaging complex amplitudes,

$$\frac{1}{T_{\text{cyc}}}\int_0^{T_{\text{cyc}}} \Re(Ae^{-i\omega t})\Re(Be^{-i\omega t})\,\mathrm{d}t = \frac{1}{2}\Re(AB^*), \qquad T_{\text{cyc}} = \frac{2\pi}{\omega}, \tag{B3}$$

where A and B are arbitrary complex amplitudes. Thus, the plotted flux fields are cycle-averaged envelope quantities, not instantaneous products of real time-domain fields.

The incident energy is obtained from a homogeneous reference run,

$$E_{\text{inc}} = \int_0^{t_{\text{end}}} [P_{\text{ref}}(t)]_+\,\mathrm{d}t, \tag{B4}$$

where $P_{\text{ref}}(t)$ is the left-monitor power in the homogeneous reference run and $[\,\cdot\,]_+$ denotes the positive-part operator,

$$[P]_+ = \max(P, 0). \tag{B5}$$

Thus, only right-going incident power is integrated. The reflected energy is extracted at the same left monitor by subtracting the reference signal,

$$E_{\text{ref}} = \int_0^{t_{\text{end}}} [-(P_{\text{scat}}(t) - P_{\text{ref}}(t))]_+\,\mathrm{d}t, \tag{B6}$$

where $P_{\text{scat}}(t)$ is the corresponding left-monitor power in the scattering run.

The transmitted energy reported in Table 2 is

$$E_{\mathrm{tr,region}} = E_{\mathrm{absorbed,right}}(t_{\mathrm{end}}) + E_{\mathrm{stored,right}}(t_{\mathrm{end}}). \tag{B7}$$

The absorbed part is the accumulated sponge work,

$$E_{\mathrm{absorbed,right}} = \int_0^{t_{\mathrm{end}}} P_{\mathrm{abs,right}}(t)\,\mathrm{d}t, \qquad P_{\mathrm{abs,right}} = \frac{1}{2}\sum_{j\in\Omega_{\mathrm{abs,right}}} \gamma_j M_{jj}|v_j|^2. \tag{B8}$$

Here $\Omega_{\mathrm{abs,right}}$ is the right absorbing region, j indexes mechanical velocity degrees of freedom in that region, γ_j is the local sponge damping coefficient, M_{jj} is the corresponding diagonal mass entry, and v_j is the associated velocity degree of freedom.

The stored part is evaluated from

$$E_{\mathrm{stored,right}} = E_{\mathrm{kin,right}} + E_{\mathrm{int,right}}, \qquad E_{\mathrm{kin,right}} = \frac{1}{4}\int_{\Omega_{\mathrm{right}}} \mathbf{v}^{\mathrm{H}}\boldsymbol{\rho}\mathbf{v}\,\mathrm{d}\Omega, \tag{B9}$$

and

$$E_{\mathrm{int,right}} = \frac{1}{4}\int_{\Omega_{\mathrm{right}}} \Re\left\{\varepsilon^{\mathrm{H}}\mathbf{C}\varepsilon + 2\varepsilon^{\mathrm{H}}\mathbf{B}^{\dagger}\mathbf{g}_{\phi} - \mathbf{g}_{\phi}^{\mathrm{H}}\mathbf{A}\mathbf{g}_{\phi}\right\}\,\mathrm{d}\Omega, \tag{B10}$$

where Ω_{right} is the right-side computational region, $\mathbf{v}$ is the mechanical velocity envelope, $\boldsymbol{\rho}$ is the mass-density tensor, and

$$\varepsilon = \nabla_{\mathrm{s},\kappa_2}\mathbf{u}, \qquad \mathbf{g}_{\phi} = \nabla_{\kappa_2}\phi = (\phi_{,1}, \phi_{,2} + i\kappa_2\phi)^{\mathsf{T}}, \tag{B11}$$

with superscript H denoting Hermitian transpose. The sign of the dielectric term follows from the use of $\nabla\phi$, rather than $\mathbf{E} = -\nabla\phi$, as the independent electric kinematic variable. The constitutive tensors are phase-wise tensors in the composite and local effective tensors in the homogeneous model.

In the effective-medium run, the Willis and electromomentum couplings enter the dynamics and the flux through

$$\boldsymbol{\sigma} = \mathbf{C}\varepsilon + \mathbf{B}^{\dagger}\mathbf{g}_{\phi} + \mathbf{S}\mathbf{v}, \qquad \mathbf{D} = \mathbf{B}\varepsilon - \mathbf{A}\mathbf{g}_{\phi} + \mathbf{W}\mathbf{v}. \tag{B12}$$

The finite-time energy bookkeeping above is used as a scattering diagnostic for the narrowband simulations. The final time is $t_{\mathrm{end}} = 3.8 \times 10^{-4}$ s for Cases 1–2 and $t_{\mathrm{end}} = 9.5 \times 10^{-4}$ s for Case 3.

The snapshots in Figs. 12–17 are generated from saved finite-element envelope states at times $t_m \simeq \alpha_m t_{\mathrm{end}}$, where m indexes the saved snapshot and $\alpha_m \in \{0.25, 0.50, 0.75\}$. The displacement panels plot the real S-polarized physical displacement

$$u_s(\mathbf{x}, t_m) = \mathrm{Re}\left\{e^{i\kappa_2 x_2}\,\mathbf{e}_s(\theta)\cdot\mathbf{u}_h(\mathbf{x}, t_m)\right\}, \qquad \mathbf{e}_s(\theta) = \begin{pmatrix} -\sin\theta \\ \cos\theta \end{pmatrix}. \tag{B13}$$

Here $\mathbf{u}_h(\mathbf{x}, t_m)$ is the finite-element displacement envelope at position $\mathbf{x} = (x_1, x_2)$ and time t_m, and $\mathbf{e}_s(\theta)$ is the unit polarization vector of the incident S wave. This signed projection preserves phase and isolates the directly excited shear component. The flux panels plot $q_{x_1}(\mathbf{x}, t_m)$ from Eq. (B2).

References

[1] Muamer Kadic, Tiemo Bückmann, Robert Schittny, and Martin Wegener. Metamaterials beyond electromagnetism. *Reports on Progress in Physics*, 76(12):126501, 2013.

[2] Muamer Kadic, Graeme W. Milton, Martin van Hecke, and Martin Wegener. 3d metamaterials. *Nature Reviews Physics*, 1(3):198–210, 2019.

[3] Richard V Craster and Sébastien Guenneau. *Acoustic metamaterials: Negative refraction, imaging, lensing and cloaking*, volume 166. Springer Science & Business Media, 2012.

[4] Hao Ge, Min Yang, Chu Ma, Ming-Hui Lu, Yan-Feng Chen, Nicholas Fang, and Ping Sheng. Breaking the barriers: advances in acoustic functional materials. *National Science Review*, 5(2):159–182, 12 2017.

[5] A Srivastava. Metamaterial properties of periodic laminates. *J. Mech. Phys. Solids*, 96:252–263, 2016.

[6] D Bigoni, S Guenneau, A B Movchan, and M Brun. Elastic metamaterials with inertial locally resonant structures: Application to lensing and localization. *Phys. Rev. B*, 87(17):174303, 2013.

[7] William J. Parnell and Tom Shearer. Antiplane elastic wave cloaking using metamaterials, homogenization and hyperelasticity. *Wave Motion*, 50(7):1140 – 1152, 2013. Advanced Modelling of Wave Propagation in Solids.

[8] Jeonghoon Park, Dongwoo Lee, and Junsuk Rho. Recent advances in non-traditional elastic wave manipulation by macroscopic artificial structures. *Applied Sciences*, 10(2), 2020.

[9] Ben Lustig, Guy Elbaz, Alan Muhafra, and Gal Shmuel. Anomalous energy transport in laminates with exceptional points. *Journal of the Mechanics and Physics of Solids*, page 103719, 2019.

[10] Ariel Fishman, Guy Elbaz, T. Venkatesh Varma, and Gal Shmuel. Third-order exceptional points and frozen modes in planar elastic laminates. *Journal of the Mechanics and Physics of Solids*, 186:105590, 2024.

[11] Simon Yves, Michel Fruchart, Romain Fleury, Gal Shmuel, Vincenzo Vitelli, Michael R. Haberman, and Andrea Alù. Symmetry-driven artificial phononic media. *Nature Reviews Materials*, 2025.

[12] Graeme W Milton. *The theory of composites*. Cambridge University press, 2002.

[13] Alain Bensoussan, Jacques-Louis Lions, and George Papanicolaou. *Asymptotic analysis for periodic structures*, volume 374. American Mathematical Soc., 2011.

[14] W J Parnell and I D Abrahams. Dynamic homogenization in periodic fibre reinforced media. Quasi-static limit for SH waves. *Wave Motion*, 43(6):474–498, 2006.

[15] I V Andrianov, V I Bolshakov, V V Danishevshtkyy, and D Weichert. Higher order asymptotic homogenization and wave propagation in periodic composite materials. *Proc. R. Soc. London A Math. Phys. Eng. Sci.*, 464(2093):1181–1201, 2008.

[16] R V Craster, J Kaplunov, and A V Pichugin. High-frequency homogenization for periodic media. *Proc. R. Soc. London A Math. Phys. Eng. Sci.*, 466(2120):2341–2362, 2010.

[17] J R Willis. Variational principles for dynamic problems for inhomogeneous elastic media. *Wave Motion*, 3(1):1–11, 1981.

[18] J R Willis. The nonlocal influence of density variations in a composite. *Int. J. Solids Struct.*, 21(7):805–817, 1985.

[19] J R Willis. Dynamics of Composites. In P Suquet, editor, *Continuum Micromechanics*, pages 265–290. Springer-Verlag New York, Inc., New York, NY, USA, 1997.

[20] J R Willis. Effective constitutive relations for waves in composites and metamaterials. *Proc. R. Soc. London A Math. Phys. Eng. Sci.*, 467(2131):1865–1879, 2011.

[21] John R. Willis. The construction of effective relations for waves in a composite. *Comptes Rendus Mécanique*, 340(4):181 – 192, 2012. Recent Advances in Micromechanics of Materials.

[22] J.R. Willis. A comparison of two formulations for effective relations for waves in a composite. *Mechanics of Materials*, 47:51 – 60, 2012.

[23] Marie-Fraise Ponge, Olivier Poncelet, and Daniel Torrent. Dynamic homogenization theory for nonlocal acoustic metamaterials. *Extrem. Mech. Lett.*, 12:71–76, 2017.

[24] Yu-Gui Peng, Yarden Mazor, and Andrea Alù. Fundamentals of acoustic willis media. *Wave Motion*, 112:102930, 2022.

[25] Anton Melnikov, Yan Kei Chiang, Li Quan, Sebastian Oberst, Andrea Alù, Steffen Marburg, and David Powell. Acoustic meta-atom with experimentally verified maximum Willis coupling. *Nature Communications*, 10(1):3148, 2019.

[26] Li Quan, Younes Ra'di, Dimitrios L Sounas, and Andrea Alù. Maximum Willis Coupling in Acoustic Scatterers. *Phys. Rev. Lett.*, 120(25):254301, 2018.

[27] Yongquan Liu, Zixian Liang, Jian Zhu, Lingbo Xia, Olivier Mondain-Monval, Thomas Brunet, Andrea Alù, and Jensen Li. Willis metamaterial on a structured beam. *Phys. Rev. X*, 9:011040, Feb 2019.

[28] Michael B Muhlestein, Caleb F Sieck, Andrea Alù, and Michael R Haberman. Reciprocity, passivity and causality in Willis materials. *Proc. R. Soc. London A Math. Phys. Eng. Sci.*, 472(2194), 2016.

[29] Caleb F Sieck, Andrea Alù, and Michael R Haberman. Origins of Willis coupling and acoustic bianisotropy in acoustic metamaterials through source-driven homogenization. *Phys. Rev. B*, 96(10):104303, 2017.

[30] Michael B. Muhlestein, Caleb F. Sieck, Preston S. Wilson, and Michael R. Haberman. Experimental evidence of Willis coupling in a one-dimensional effective material element. *Nature Communications*, 8:15625 EP –, 06 2017.

[31] René Pernas-Salomón and Gal Shmuel. Symmetry breaking creates electro-momentum coupling in piezoelectric metamaterials. *Journal of the Mechanics and Physics of Solids*, 134:103770, 2020.

[32] René Pernas-Salomón and Gal Shmuel. Fundamental principles for generalized Willis metamaterials. *Phys. Rev. Applied*, 14:064005, Dec 2020.

[33] René Pernas-Salomón, Michael R. Haberman, Andrew N. Norris, and Gal Shmuel. The electromomentum effect in piezoelectric Willis scatterers. *Wave Motion*, page 102797, 2021.

[34] Alan Muhafra, Majd Kosta, Daniel Torrent, René Pernas-Salomón, and Gal Shmuel. Homogenization of piezoelectric planar Willis materials undergoing antiplane shear. *Wave Motion*, 108:102833, 2022.

[35] Kevin Muhafra, Michael R. Haberman, and Gal Shmuel. Discrete one-dimensional models for the electromomentum coupling. *Phys. Rev. Appl.*, 20:014042, Jul 2023.

[36] Majd Kosta, Alan Muhafra, Rene Pernas-Salómon, Gal Shmuel, and Oded Amir. Maximizing the electromomentum coupling in piezoelectric laminates. *International Journal of Solids and Structures*, 254-255:111909, 2022.

[37] Jeong-Ho Lee, Zhizhou Zhang, and Grace X Gu. Maximum electro-momentum coupling in piezoelectric metamaterial scatterers. *Journal of Applied Physics*, 132(12):125108, 2022.

[38] Jeong-Ho Lee, Zhizhou Zhang, and Grace X. Gu. Dynamic homogenization of heterogeneous piezoelectric media: A polarization approach using infinite-body green's function. *Journal of the Mechanics and Physics of Solids*, 181:105442, 2023.

[39] Chirag A. Gokani, Samuel P. Wallen, Mark F. Hamilton, and Michael R. Haberman. Source-driven homogenization theory for electro-momentum coupled scatterers. *The Journal of the Acoustical Society of America*, March 2023. Meeting abstract.

[40] Samuel P. Wallen, Benjamin M. Goldsberry, Chirag A. Gokani, and Michael R. Haberman. Computational analysis of sub-wavelength scatterers exhibiting electro-momentum coupling. *The Journal of the Acoustical Society of America*, 153(3 Suppl.):A120, 2023. Meeting abstract; 184th Meeting of the Acoustical Society of America (ASA), Chicago, IL.

[41] Matthew A. Casali, Andrew R. McNeese, Samuel P. Wallen, and Michael R. Haberman. Impedance tube method for characterization of one-dimensional electro-momentum coupled materials. *The Journal of the Acoustical Society of America*, 152(4_Supplement):A234, 2022. Meeting abstract; 183rd Meeting of the Acoustical Society of America, Nashville, TN, USA (Dec. 8, 2022), Session 4aSAb1.

[42] Hai D. Huynh, Xiaoying Zhuang, Harold S. Park, S.S. Nanthakumar, Yabin Jin, and Timon Rabczuk. Maximizing electro-momentum coupling in generalized 2d Willis metamaterials. *Extreme Mechanics Letters*, 61:101981, 2023.

[43] Chirag A. Gokani, Samuel P. Wallen, and Michael R. Haberman. Reciprocity, passivity, and causality in fully coupled acousto-electrodynamic media. *The Journal of the Acoustical Society of America*, 154(4_Supplement):A118, October 2023. Meeting abstract.

[44] Zhizhou Zhang, Jeong-Ho Lee, and Grace X. Gu. Rational design of piezoelectric metamaterials with tailored electro-momentum coupling. *Extreme Mechanics Letters*, 55:101785, 2022.

[45] Hrishikesh Danawe and Serife Tol. Electro-momentum coupling tailored in piezoelectric metamaterials with resonant shunts. *APL Materials*, 11(9):091118, 09 2023.

[46] Hrishikesh Danawe and Serife Tol. Unidirectional zero reflection and perfect absorption via exceptional points in active piezoelectric willis metamaterials, 2025.

[47] Hai D. Huynh, S.S. Nanthakumar, Harold S. Park, Timon Rabczuk, and Xiaoying Zhuang. The effect of electro-momentum coupling on unidirectional zero reflection in layered generalized willis metamaterials. *Extreme Mechanics Letters*, 77:102318, 2025.

[48] A. Baz. Why active willis metamaterials? a controllability and observability perspective. *The Journal of the Acoustical Society of America*, 156(5):3338–3352, 2024.

[49] A. Baz. Bandgap, dispersion, and non-reciprocal characteristics of an active willis metamaterial. *The Journal of the Acoustical Society of America*, 158(1), 2025. In press (DOI and page range not found in accessible sources at time of lookup).

[50] Gal Shmuel and John R. Willis. Thermally bianisotropic metamaterials induced by spatial asymmetry. *Phys. Rev. Lett.*, 135:116303, Sep 2025.

[51] Gal Shmuel and John R. Willis. Exact homogenization method for heat conduction. *Phys. Rev. Appl.*, 25:014072, Jan 2026.

[52] M M Sigalas and E N Economou. Elastic and acoustic wave band structure. *J. Sound Vib.*, 158(2):377–382, 1992.

[53] M S Kushwaha, P Halevi, L Dobrzynski, and B Djafari-Rouhani. Acoustic band structure of periodic elastic composites. *Phys. Rev. Lett.*, 71(13):2022–2025, 1993.

[54] R Getz, D M Kochmann, and G Shmuel. Voltage-controlled complete stopbands in two-dimensional soft dielectrics. *Int. J. Solids Struct.*, 113–114:24–36, 2017.

[55] R Getz and G Shmuel. Band gap tunability in deformable dielectric composite plates. *Int. J. Solids Struct.*, 2017.

[56] Zvi Hashin. Analysis of composite materials—a survey. *Journal of Applied Mechanics*, 50(3):481–505, 1983.

[57] Ankit Srivastava. Elastic metamaterials and dynamic homogenization: a review. *International Journal of Smart and Nano Materials*, 6(1):41–60, 2015.

[58] Chris Fietz and Gennady Shvets. Current-driven metamaterial homogenization. *Physica B: Condensed Matter*, 405(14):2930 – 2934, 2010. Proceedings of the Eighth International Conference on Electrical Transport and Optical Properties of Inhomogeneous Media.

[59] Andrea Alù. First-principles homogenization theory for periodic metamaterials. *Phys. Rev. B*, 84:075153, Aug 2011.

[60] H. Nassar, Q.-C. He, and N. Auffray. Willis elastodynamic homogenization theory revisited for periodic media. *Journal of the Mechanics and Physics of Solids*, 77:158–178, 2015.

[61] Andrea Alù. Restoring the physical meaning of metamaterial constitutive parameters. *Phys. Rev. B*, 83:081102, Feb 2011.

[62] Ankit Srivastava. Causality and passivity in elastodynamics. *Proceedings of the Royal Society of London A: Mathematical, Physical and Engineering Sciences*, 471(2180), 2015.

[63] A Srivastava and S Nemat-Nasser. On the limit and applicability of dynamic homogenization. *Wave Motion*, 51(7):1045–1054, 2014.

[64] René Pernas-Salomón and Gal Shmuel. Dynamic homogenization of composite and locally resonant flexural systems. *J. Mech. Phys. Solids*, 119:43–59, 2018.

[65] L M Joseph and R V Craster. Reflection from a semi-infinite stack of layers using homogenization. *Wave Motion*, 54:145–156, 2015.

[66] Samuel P. Wallen, Benjamin M. Goldsberry, Chirag A. Gokani, and Michael R. Haberman. Computational analysis of sub-wavelength scatterers exhibiting electro-momentum coupling. *The Journal of the Acoustical Society of America*, 153:A120–A120, 03 2023.

[67] C R Simovski. On electromagnetic characterization and homogenization of nanostructured metamaterials. *Journal of Optics*, 13(1):013001, nov 2010.